ICAS 2021 SHANGHAI
International Council of the Aeronautical Sciences
32nd Congress of the International Council of the Aeronautical Sciences
September 6-10, 2021
Pudong Shangri-La, Shanghai, China

ROBUST CONTROL OF UNMANNED AERIAL VEHICLE WITH TILT ROTORS AND CAMERA

T. L. Costa[1], J. C. Vendrichoski[1], E. S. El'Youssef[2] & E. R. De Pieri[1]

[1]Automation and System Department, Federal University of Santa Catarina, Florianopolis, Santa Catarina, Brazil
[2]Federal University of Santa Catarina, Blumenau, Santa Catarina, Brazil

Abstract

In this work, we present a UAV with an H-shaped structure with four tilt rotors and equipped with a camera. We develop the complete dynamic model, which is used for numerical simulations. We also design a simplified dynamic model, which is formulated to facilitate the control system design. In the following, we develop a control system to UAV tracks feasible trajectories and orientate the camera, even in the presence of external disturbances and perturbations, such as wind gusts and modeling errors. To control the UAV position, we use the robust H_∞ control technique and a dynamic inverse to compensate for the nonlinearities. To control the UAV attitude, rotors inclination, and camera pointing, we use the Generalized Super-Twisting Algorithm control technique and compensation of the nonlinearities. To analyze the system performance, we realize numerical simulations, where we verified a satisfactory performance.

Keywords: UAV, H-Shaped Quadrotor, Sliding Mode Control, Robust Control

1. Introduction

The use of unmanned aerial vehicles (UAVs) has been shown very advantageous. Since replacing the manned aerial vehicles, we can have a cost reduction and perform previously unfeasible tasks.
The UAV we use in this work is the H-shaped quad tilt-rotor, which has the four rotors positioned, forming an H-shape (see Figure 1). With this structure, the UAV has direct actuation in two directions; which allows it to take off and land vertically and move forward/backward without inclining. This structure, which is little explored, shows advantages in tasks requiring high speeds or a coupled tool. An example of a task is surveillance. In this case, besides being composed of vigilant and fixed cameras, it also would have mobile cameras, increasing the coverage area and adding the possibility of following a target. Concerning the system structure, we can couple a camera to the UAV body through a gimbal mechanism, which offers more degrees of freedom for the camera movement. In this work, we use a gimbal with two degrees of freedom, as shown in Figure 1.
Also, we can add robust controllers to the whole system, aggregating robustness in situations in which the UAV is exposed to external disturbances.
Concerning the control systems, we found few works related to the H-shaped quad tilt rotor. In [1], is developed a control system for an H-shaped quad tilt rotor equipped with a camera aimed for racing purposes using PID controller, whose gains were tuned through genetic algorithm. Besides, 1 considered the rotors to move equally.
However, for others UAVs structures, we verify in the literature that control systems is a lot explored theme. This can be seen in [2–4], where were realized reviews of control techniques applied in UAVs. In these works, the UAV most used is the quad rotor in X-shape structure. Several control techniques have been used such as PID [5], LQR [6], robust control H_∞ [7], feedback linearization [8–10], backstepping [6,7], sliding mode control (SMC) [11–15], and intelligent control system techniques [1,4]. After some analysis of the system response, robustness, and control effort, we concluded that, in general, the SMC presented the best performance [2–4].

The SMC is a robust nonlinear control technique that has been widely used. The conventional one, the first-order SMC, has the disadvantage of generating chattering, which is caused due to the discontinuity presented in the control signal. We can use the high-order SMC (HOSMC), characterized by a continuous control signal, whose times derivatives are discontinuous, to deal with this issue. Then, the chattering is attenuated, and the robustness is maintained [16].
As an example of a HOSMC methodology, we can cite the super-twisting algorithm (STA) [17]. This control technique is characterized by a continuous control signal with the first-time derivative discontinuous. Moreno and Osorio [18] analyzed this control signal robustness and verified that it has a strong action near the origin than far from there, dealing better with disturbances that act near the origin. Moreno [19] proposed a variation of the STA, known as generalized super-twisting algorithm (GSTA), by adding terms that grow over time. Then, besides having a strong actuation near the origin, it also has the capability of a strong action far from there, dealing with a large class of disturbances.
In this work, we develop a control system for the H-shaped quad tilt rotor equipped with a camera presented in Figure 1 to track trajectories as well as to guide the camera even in the presence of external disturbances, such as wind gusts. Some of our preliminary works are presented in [20, 21].
The paper is organized as follows. In Section 2. we present briefly the complete and the simplified dynamic models, which is used for the control design. In Section 3. we present the control system development. In Section 4. we presented the results performed through numerical simulations. In Section 5. we present the work conclusions and proposes for future works.

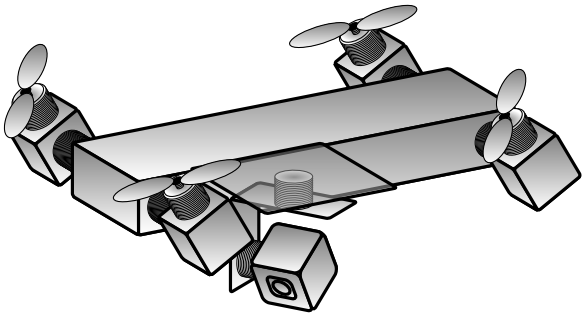

Figure 1 – H-shaped quad tilt rotor.

2. System Model

In this Section, we use small letters to represent scalar variables, bold small letters to represent vectors and bold capital letters to indicate matrices. We also consider the representation $s_* = sin(*)$ and $c_* = cos(*)$.
To model the system, we fix coordinates systems in each body of the system. As we can see in Figure 2, the coordinates frames $\mathfrak{B}$, $\mathfrak{C}_1$, $\mathfrak{C}_2$, $\mathfrak{C}_3$, $\mathfrak{C}_4$, and $\mathfrak{C}_5$ are fixed in the center of mass of the UAV body, rotors $1,\ 2,\ 3,\ 4$ and the gimbal, respectively.
We choose as generalized coordinates vector $\boldsymbol{q} = \begin{bmatrix}\boldsymbol{\xi}^T & \boldsymbol{\eta}^T & \boldsymbol{\alpha}^T & \boldsymbol{\gamma}^T\end{bmatrix}^T \in \mathbb{R}^{12\times 1}$, where $\boldsymbol{\xi} = \begin{bmatrix}x & y & z\end{bmatrix}^T$ and $\boldsymbol{\eta} = \begin{bmatrix}\phi & \theta & \psi\end{bmatrix}^T$ represent the UAV position and attiude, respectively, $\boldsymbol{\alpha} = \begin{bmatrix}\alpha_1 & \alpha_2 & \alpha_3 & \alpha_4\end{bmatrix}^T$ represents the rotors inclination and $\boldsymbol{\gamma} = \begin{bmatrix}\gamma_1 & \gamma_2\end{bmatrix}^T$ represents the gimbal movement.

2.1 Kinematic Model

Using the Euler angles formalism and considering the generalized coordinates $\boldsymbol{\eta}$, we obtain as rotation matrix [22]

$$\boldsymbol{R}_{\mathfrak{B}}^{\mathfrak{I}} = \left(\boldsymbol{R}_{\mathfrak{B}_{\boldsymbol{z},\boldsymbol{\psi}}}\right)\left(\boldsymbol{R}_{\mathfrak{B}_{\boldsymbol{y},\boldsymbol{\theta}}}\right)\left(\boldsymbol{R}_{\mathfrak{B}_{\boldsymbol{x},\boldsymbol{\phi}}}\right) = \begin{bmatrix} c_\psi c_\theta & c_\psi s_\theta s_\phi - s_\psi c_\phi & c_\psi s_\theta c_\phi + s_\psi s_\phi \\ s_\psi c_\theta & s_\psi s_\theta s_\phi + c_\psi c_\phi & s_\psi s_\theta c_\phi - c_\psi s_\phi \\ -s_\theta & c_\theta s_\phi & c_\theta c_\phi \end{bmatrix}, \tag{1}$$

where $\boldsymbol{R}_{\mathfrak{B}}^{\mathfrak{I}}$ represents the relation between the orientations of $\mathfrak{I}$ and $\mathfrak{B}$.

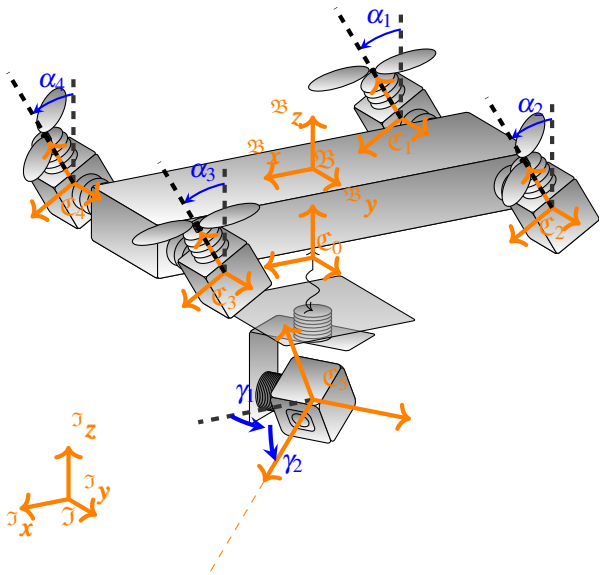

Figure 2 – UAV with coordinates frames.

As the rotor i moves around ${}^{\mathfrak{C}_i}y$ and using the Euler angles representation, we have

$$\boldsymbol{R}_{\mathfrak{C}_i}^{\mathfrak{B}} = \left(\boldsymbol{R}_{\mathfrak{C}_i \boldsymbol{y}, \boldsymbol{\alpha_i}}\right) = \begin{bmatrix} c_{\alpha_i} & 0 & s_{\alpha_i} \\ 0 & 1 & 0 \\ -s_{\alpha_i} & 0 & c_{\alpha_i} \end{bmatrix}, \tag{2}$$

for $i = 1,\ 2,\ 3,\ 4$.
With regard to the gimbal, it moves around ${}^{\mathfrak{C}_5}y$ and ${}^{\mathfrak{C}_5}z$. Representing these movements respectively by the angles γ_1 and γ_2 and using the Euler angles representation, we have

$$\boldsymbol{R}_{\mathfrak{C}_5}^{\mathfrak{B}} = \left(\boldsymbol{R}_{\mathfrak{C}_5 y, \boldsymbol{\gamma_2}}\right)\left(\boldsymbol{R}_{\mathfrak{B} z, \boldsymbol{\gamma_1}}\right) = \begin{bmatrix} c_{\gamma_1} c_{\gamma_2} & -s_{\gamma_1} & c_{\gamma_1} s_{\gamma_2} \\ s_{\gamma_1} c_{\gamma_2} & c_{\gamma_1} & s_{\gamma_1} s_{\gamma_2} \\ -s_{\gamma_2} & 0 & c_{\gamma_2} \end{bmatrix}, \tag{3}$$

where $\boldsymbol{R}_{\mathfrak{C}_5}^{\mathfrak{B}}$ transforms the orientation of $\mathfrak{C}_5$ to $\mathfrak{B}$.
We achieve the kinematics relations by deriving with respect to time the relations in (1), (2) and (3), obtaining

$$\dot{\boldsymbol{R}}_{\mathfrak{B}}^{\mathfrak{I}} = \boldsymbol{R}_{\mathfrak{B}}^{\mathfrak{I}} \boldsymbol{S}(\boldsymbol{\omega}_{\mathfrak{B}}^{\mathfrak{I}}), \tag{4}$$

$$\dot{\boldsymbol{R}}_{\mathfrak{C}_i}^{\mathfrak{B}} = \boldsymbol{R}_{\mathfrak{C}_i}^{\mathfrak{B}} \boldsymbol{S}(\boldsymbol{\omega}_{\mathfrak{C}_i}^{\mathfrak{B}}), \tag{5}$$

$$\dot{\boldsymbol{R}}_{\mathfrak{C}_5}^{\mathfrak{B}} = \boldsymbol{R}_{\mathfrak{C}_5}^{\mathfrak{B}} \boldsymbol{S}(\boldsymbol{\omega}_{\mathfrak{C}_5}^{\mathfrak{B}}), \tag{6}$$

for $i = 1,\ 2,\ 3,\ 4$, where $\boldsymbol{\omega}_{\mathfrak{B}}^{\mathfrak{I}} = \begin{bmatrix} \omega_{\mathfrak{B}_x}^{\mathfrak{I}} & \omega_{\mathfrak{B}_y}^{\mathfrak{I}} & \omega_{\mathfrak{B}_z}^{\mathfrak{I}} \end{bmatrix}^T$, $\boldsymbol{\omega}_{\mathfrak{C}_i}^{\mathfrak{B}} = \begin{bmatrix} \omega_{\mathfrak{C}_{ix}}^{\mathfrak{B}} & \omega_{\mathfrak{C}_{iy}}^{\mathfrak{B}} & \omega_{\mathfrak{C}_{iz}}^{\mathfrak{B}} \end{bmatrix}^T$, and $\boldsymbol{\omega}_{\mathfrak{C}_5}^{\mathfrak{B}} = \begin{bmatrix} \omega_{\mathfrak{C}_{5x}}^{\mathfrak{B}} & \omega_{\mathfrak{C}_{5y}}^{\mathfrak{B}} & \omega_{\mathfrak{C}_{5z}}^{\mathfrak{B}} \end{bmatrix}^T$ are the angular velocity in $\mathfrak{B}$, $\mathfrak{C}_i$, and $\mathfrak{C}_5$, respectively. The matrices $\boldsymbol{S}(\boldsymbol{\omega}_{\mathfrak{B}}^{\mathfrak{I}})$, $\boldsymbol{S}(\boldsymbol{\omega}_{\mathfrak{C}_i}^{\mathfrak{B}})$, and $\boldsymbol{S}(\boldsymbol{\omega}_{\mathfrak{C}_5}^{\mathfrak{B}})$ are skew-symmetric matrices [**?**]. Manipulating (4), (5) and (6), we obtain the following relations

$$\boldsymbol{\omega}_{\mathfrak{B}}^{\mathfrak{I}} = \begin{bmatrix} 1 & 0 & -s_\theta \\ 0 & c_\phi & c_\theta s_\phi \\ 0 & -s_\phi & c_\theta c_\phi \end{bmatrix} \begin{bmatrix} \dot{\phi} \\ \dot{\theta} \\ \dot{\psi} \end{bmatrix} = \boldsymbol{W}_{\boldsymbol{\eta}} \dot{\boldsymbol{\eta}}, \tag{7}$$

$$\boldsymbol{\omega}_{\mathfrak{C}_i}^{\mathfrak{B}} = \begin{bmatrix} 0 \\ 1 \\ 0 \end{bmatrix} \dot{\alpha}_i = \boldsymbol{w}_{\boldsymbol{\alpha}} \dot{\alpha}, \tag{8}$$

$$\boldsymbol{\omega}_{\mathfrak{C}_5}^{\mathfrak{B}} = \begin{bmatrix} -s_{\gamma_2} & 0 \\ 0 & 1 \\ C_{\gamma_2} & 0 \end{bmatrix} \begin{bmatrix} \dot{\gamma}_1 \\ \dot{\gamma}_2 \end{bmatrix} = \boldsymbol{W}_{\boldsymbol{\gamma}} \dot{\boldsymbol{\gamma}}. \tag{9}$$

To obtain the linear velocity, consider a point P_i located at ${}^{\mathfrak{C}_i}\boldsymbol{p}_{\boldsymbol{i}} = \begin{bmatrix} {}^{\mathfrak{C}_i}p_{x_i} & {}^{\mathfrak{C}_i}p_{y_i} & {}^{\mathfrak{C}_i}p_{z_i} \end{bmatrix}^T$ in $\mathfrak{C}_i$, for $i = 0,\ 1,\ 2,\ 3,\ 4,\ 5$. Considering ${}^{\mathfrak{C}_i}\boldsymbol{p}_{\boldsymbol{i}}$, we describe the location of P_i in $\mathfrak{I}$ as

$${}^{\mathfrak{I}}\boldsymbol{p}_{\boldsymbol{i}} = \boldsymbol{R}_{\mathfrak{B}}^{\mathfrak{I}} \left(\boldsymbol{R}_{\mathfrak{C}_i}^{\mathfrak{B}} {}^{\mathfrak{C}_i}\boldsymbol{p}_{\boldsymbol{i}} + \boldsymbol{d}_{\mathfrak{C}_i}^{\mathfrak{B}} \right) + \boldsymbol{\xi}, \tag{10}$$

where $\boldsymbol{d}_{\mathfrak{C}_i}^{\mathfrak{B}} = \begin{bmatrix} d_{\mathfrak{C}_{ix}}^{\mathfrak{B}} & d_{\mathfrak{C}_{iy}}^{\mathfrak{B}} & d_{\mathfrak{C}_{iz}}^{\mathfrak{B}} \end{bmatrix}^T$ is the distance between $\mathfrak{C}_i$ and $\mathfrak{B}$, for $i = 0,\ 1,\ 2,\ 3,\ 4,\ 5$. Being the relations (4), (5) and (6), we derive (10) with respect to time, obtaining

$${}^{\mathfrak{I}}\boldsymbol{v}_{\boldsymbol{i}} = {}^{\mathfrak{I}}\dot{\boldsymbol{p}}_{\boldsymbol{i}} = \boldsymbol{R}_{\mathfrak{B}}^{\mathfrak{I}} \boldsymbol{S}(\boldsymbol{\omega}_{\mathfrak{B}}^{\mathfrak{I}}) \left(\boldsymbol{R}_{\mathfrak{C}_i}^{\mathfrak{B}} {}^{\mathfrak{C}_i}\boldsymbol{p}_{\boldsymbol{i}} + \boldsymbol{d}_{\mathfrak{C}_i}^{\mathfrak{B}} \right) + \boldsymbol{R}_{\mathfrak{B}}^{\mathfrak{I}} \boldsymbol{R}_{\mathfrak{C}_i}^{\mathfrak{B}} \boldsymbol{S}(\boldsymbol{\omega}_{\mathfrak{C}_i}^{\mathfrak{B}}) {}^{\mathfrak{C}_i}\boldsymbol{p}_{\boldsymbol{i}} + \dot{\boldsymbol{\xi}}, \tag{11}$$

for $i = 0,\ 1,\ 2,\ 3,\ 4,\ 5$.

2.2 Complete Dynamic Model

In this section, we develop the complete dynamic model of the H-shaped quad tilt rotor equipped with a camera using the Euler-Lagrange formalism.
We can describe the system model with the following structure

$$\boldsymbol{M}(\boldsymbol{q})\ddot{\boldsymbol{q}} + \boldsymbol{C}(\boldsymbol{q}, \dot{\boldsymbol{q}})\dot{\boldsymbol{q}} + \boldsymbol{g}(\boldsymbol{q}) = \boldsymbol{f}(\boldsymbol{q}) + \boldsymbol{f}_{\boldsymbol{d}}, \tag{12}$$

where $\boldsymbol{M}(\boldsymbol{q}) \in \mathbb{R}^{12\times12}$ is the inertia matrix, $\boldsymbol{C}(\boldsymbol{q}, \dot{\boldsymbol{q}}) \in \mathbb{R}^{12\times12}$ is the centrifugal and Coriolis forces, $\boldsymbol{g}(\boldsymbol{q}) \in \mathbb{R}^{12\times1}$ is the gravitational vector, $\boldsymbol{f} \in \mathbb{R}^{12\times1}$ is the forces vector that affects the generalized coordinates, and $\boldsymbol{f}_{\boldsymbol{d}} \in \mathbb{R}^{12\times1}$ is the disturbance force vector.
Considering the velocity in (11), we obtain the inertia matrix through the kinetic energy $\mathscr{K}(\boldsymbol{q}, \dot{\boldsymbol{q}})$ as

$$\mathscr{K}(\boldsymbol{q}, \dot{\boldsymbol{q}}) = \sum_{i=0}^{5} \left(\frac{1}{2} \int {}^{\mathfrak{I}}\boldsymbol{v}_{\boldsymbol{i}}^T {}^{\mathfrak{I}}\boldsymbol{v}_{\boldsymbol{i}} dm_i \right) = \frac{1}{2} \dot{\boldsymbol{q}}^T \boldsymbol{M}(\boldsymbol{q}) \dot{\boldsymbol{q}}. \tag{13}$$

From (13), we obtain a inertia with the following structure

$$\boldsymbol{M}(\boldsymbol{q}) = \begin{bmatrix} \boldsymbol{M}_{\boldsymbol{\xi}} & \boldsymbol{M}_{\boldsymbol{\xi},\boldsymbol{\eta}} & \mathbb{O}_{3\times4} & \mathbb{O}_{3\times2} \\ \boldsymbol{M}_{\boldsymbol{\xi},\boldsymbol{\eta}}^T & \boldsymbol{M}_{\boldsymbol{\eta}} & \boldsymbol{M}_{\boldsymbol{\eta},\boldsymbol{\alpha}} & \boldsymbol{M}_{\boldsymbol{\eta},\boldsymbol{\gamma}} \\ \mathbb{O}_{4\times3} & \boldsymbol{M}_{\boldsymbol{\eta},\boldsymbol{\alpha}}^T & \boldsymbol{M}_{\boldsymbol{\alpha}} & \mathbb{O}_{4\times2} \\ \mathbb{O}_{2\times3} & \boldsymbol{M}_{\boldsymbol{\eta},\boldsymbol{\gamma}}^T & \mathbb{O}_{2\times4} & \boldsymbol{M}_{\boldsymbol{\gamma}} \end{bmatrix}, \tag{14}$$

where $\mathbb{O}_{m\times n} \in \mathbb{R}^{m\times n}$ indicates a matrix of zero, and with

$\boldsymbol{M}_{\boldsymbol{\xi}} = m_t \mathbb{I}_{3\times3} \in \mathbb{R}^{3\times3}$,
$\boldsymbol{M}_{\boldsymbol{\xi},\boldsymbol{\eta}} = \boldsymbol{R}_{\mathfrak{B}}^{\mathfrak{I}} \boldsymbol{H} \boldsymbol{W}_{\boldsymbol{\eta}} \in \mathbb{R}^{3\times3}$,
$\boldsymbol{M}_{\boldsymbol{\eta}} = \boldsymbol{W}_{\boldsymbol{\eta}} \boldsymbol{J}_{\mathfrak{B}} \boldsymbol{W}_{\boldsymbol{\eta}} \in \mathbb{R}^{3\times3}$,
$\boldsymbol{M}_{\boldsymbol{\eta},\boldsymbol{\alpha}} = \boldsymbol{W}_{\boldsymbol{\eta}}^T \begin{bmatrix} \boldsymbol{R}_{\mathfrak{C}_1}^{\mathfrak{B}} \boldsymbol{I}_{\mathfrak{C}_1} & \boldsymbol{R}_{\mathfrak{C}_2}^{\mathfrak{B}} \boldsymbol{I}_{\mathfrak{C}_2} & \boldsymbol{R}_{\mathfrak{C}_3}^{\mathfrak{B}} \boldsymbol{I}_{\mathfrak{C}_3} & \boldsymbol{R}_{\mathfrak{C}_4}^{\mathfrak{B}} \boldsymbol{I}_{\mathfrak{C}_4} \end{bmatrix} \boldsymbol{w}_{\boldsymbol{\alpha}} \in \mathbb{R}^{3\times4}$,
$\boldsymbol{M}_{\boldsymbol{\alpha}} = \boldsymbol{w}_{\alpha}^T \left(diag \left(\boldsymbol{I}_{\mathfrak{C}_1}, \boldsymbol{I}_{\mathfrak{C}_2}, \boldsymbol{I}_{\mathfrak{C}_3}, \boldsymbol{I}_{\mathfrak{C}_4} \right) \right) \boldsymbol{w}_{\alpha} \in \mathbb{R}^{4\times4}$,
$\boldsymbol{M}_{\boldsymbol{\eta},\boldsymbol{\gamma}} = \boldsymbol{W}_{\boldsymbol{\eta}}^T \boldsymbol{R}_{\mathfrak{C}_5}^{\mathfrak{B}} \boldsymbol{I}_{\mathfrak{C}_5} \boldsymbol{W}_{\boldsymbol{\gamma}} \in \mathbb{R}^{3\times2}$,
$\boldsymbol{M}_{\boldsymbol{\gamma}} = \boldsymbol{W}_{\boldsymbol{\gamma}}^T \boldsymbol{I}_{\mathfrak{C}_5} \boldsymbol{W}_{\boldsymbol{\gamma}} \in \mathbb{R}^{2\times2}$,

where $\boldsymbol{I}_{\mathfrak{C}_i}$ is the inertia matrix, m_i is mass of the body i, and

$$
\begin{aligned}
&m_t = \textstyle\sum_{i=0}^{5} m_i, \\
&\boldsymbol{J}_{\mathfrak{B}} = \textstyle\sum_{i=0}^{5} \boldsymbol{J}_{\mathfrak{B}_i} = \sum_{i=0}^{5} \left(\boldsymbol{R}_{\mathfrak{C}_i}^{\mathfrak{B}} \boldsymbol{I}_{\mathfrak{C}_i} \left(\boldsymbol{R}_{\mathfrak{C}_i}^{\mathfrak{B}} \right)^T + m_i \boldsymbol{S}(\boldsymbol{d}_{\mathfrak{C}_i}^{\mathfrak{B}})^T \boldsymbol{S}(\boldsymbol{d}_{\mathfrak{C}_i}^{\mathfrak{B}}) \right), \\
&\boldsymbol{H} = -\textstyle\sum_{i=0}^{5} m_i \boldsymbol{S}(\boldsymbol{d}_{\mathfrak{C}_i}^{\mathfrak{B}}),
\end{aligned}
$$

for $i = 0,\ 1,\ 2,\ 3,\ 4,\ 5$.
To obtain the centrifugal and Coriolis matrix, we use the Christoffel symbols of the first kind, as follows [22]

$$
c_{kj} = \frac{1}{2} \sum_{i=1} 12 \left(\frac{\partial m_{kj}}{\partial q_i} + \frac{\partial m_{ki}}{\partial q_i} - \frac{\partial m_{ij}}{\partial q_k} \right) \dot{q}_i, \tag{15}
$$

where $m_{k,j}$ and $c_{k,j}$ are the (k,j)-th elements of the matrices $\boldsymbol{M}(\boldsymbol{q})$ and $\boldsymbol{C}(\boldsymbol{q},\dot{\boldsymbol{q}})$, respectively. We structure $\boldsymbol{C}(\boldsymbol{q},\dot{\boldsymbol{q}})$ as

$$
\boldsymbol{C}(\boldsymbol{q},\dot{\boldsymbol{q}}) = \begin{bmatrix}
\mathbb{O}_{3\times3} & \boldsymbol{C}_{\boldsymbol{\xi},\boldsymbol{\eta}} & \mathbb{O}_{3\times4} & \mathbb{O}_{3\times2} \\
\mathbb{O}_{3\times3} & \boldsymbol{C}_{\boldsymbol{\eta}} & \boldsymbol{C}_{\boldsymbol{\eta},\boldsymbol{\alpha}} & \boldsymbol{C}_{\boldsymbol{\eta},\boldsymbol{\gamma}} \\
\mathbb{O}_{4\times3} & \boldsymbol{C}_{\boldsymbol{\alpha},\boldsymbol{\eta}} & \mathbb{O}_{4\times4} & \mathbb{O}_{4\times2} \\
\mathbb{O}_{2\times3} & \boldsymbol{C}_{\boldsymbol{\gamma},\boldsymbol{\eta}} & \mathbb{O}_{2\times4} & \boldsymbol{C}_{\boldsymbol{\gamma}}
\end{bmatrix}. \tag{16}
$$

We obtain the gravitational vector through the potential energy $\mathscr{U}(\boldsymbol{q})$ as $\boldsymbol{g}(\boldsymbol{q}) = \frac{\partial \mathscr{U}(\boldsymbol{q})}{\partial \boldsymbol{q}}$, where

$$
\mathscr{U}(\boldsymbol{q}) = \sum_{i=0}^{5} -g\hat{\boldsymbol{k}} \left(\boldsymbol{\xi} m_i + \boldsymbol{R}_{\mathfrak{B}}^{\mathfrak{I}} \boldsymbol{d}_{\mathfrak{C}_i}^{\mathfrak{B}} m_i \right), \tag{17}
$$

with $\hat{\boldsymbol{k}} = \begin{bmatrix} 0 & 0 & 1 \end{bmatrix}^T$ and where g is the gravity acceleration. The structure of $\boldsymbol{g}(\boldsymbol{q})$ is

$$
\boldsymbol{g}(\boldsymbol{q}) = \begin{bmatrix}
\boldsymbol{g}_{\boldsymbol{\xi}} \\ \boldsymbol{g}_{\boldsymbol{\eta}} \\ \mathbb{O}_{4\times1} \\ \mathbb{O}_{2\times1}
\end{bmatrix}. \tag{18}
$$

The vector $\boldsymbol{f}(\boldsymbol{q}) = \begin{bmatrix} \boldsymbol{f}^{\mathfrak{I}^T} & \boldsymbol{\tau}_{\boldsymbol{\eta}}^T & \boldsymbol{\tau}_{\boldsymbol{\alpha}}^T & \boldsymbol{\tau}_{\boldsymbol{\gamma}}^T \end{bmatrix}^T$ is composed by the forces $\boldsymbol{f}^{\mathfrak{I}} = \begin{bmatrix} f_x^{\mathfrak{I}} & f_y^{\mathfrak{I}} & f_z^{\mathfrak{I}} \end{bmatrix}^T$ and torques $\boldsymbol{\tau}_{\boldsymbol{\eta}}^T = \begin{bmatrix} \tau_\phi & \tau_\theta & \tau_\psi \end{bmatrix}^T$ generated from the propellers forces $\boldsymbol{f}_{\boldsymbol{p}} = \begin{bmatrix} f_{p_1} & f_{p_2} & f_{p_3} & f_{p_4} \end{bmatrix}^T$. It also contains the torques of the rotors $\boldsymbol{\tau}_{\boldsymbol{\alpha}} = \begin{bmatrix} \tau_{\alpha_1} & \tau_{\alpha_2} & \tau_{\alpha_3} & \tau_{\alpha_4} \end{bmatrix}^T$ and the torque of the gimbal $\boldsymbol{\tau}_{\boldsymbol{\alpha}} = \begin{bmatrix} \tau_{\gamma_1} & \tau_{\gamma_2} \end{bmatrix}^T$.
There is component of each propeller force in ${}^{\mathfrak{B}}x$ and ${}^{\mathfrak{B}}z$ directions. We also have torque due to the distance between the propeller location and $\mathfrak{B}$ origin, and due to the drag on the propellers. Being k_τ and k_e the drag and thrust coefficients, respectively, we write the following relations to consider all the forces and torques generated by the propellers

$$
\boldsymbol{f}^{\mathfrak{I}} = \boldsymbol{R}_{\mathfrak{B}}^{\mathfrak{I}} \boldsymbol{f}^{\mathfrak{B}} = \boldsymbol{R}_{\mathfrak{B}}^{\mathfrak{I}} \begin{bmatrix} \boldsymbol{b}_{\boldsymbol{a_1}} & \boldsymbol{b}_{\boldsymbol{a_2}} & \boldsymbol{b}_{\boldsymbol{a_3}} & \boldsymbol{b}_{\boldsymbol{a_4}} \end{bmatrix} \boldsymbol{f}_{\boldsymbol{p}}, \tag{19}
$$

$$
\boldsymbol{\tau}^{\mathfrak{I}} = \boldsymbol{W}_{\boldsymbol{\eta}}^T \boldsymbol{\tau}^{\mathfrak{B}} = \boldsymbol{W}_{\boldsymbol{\eta}}^T \begin{bmatrix} \boldsymbol{b}_{\boldsymbol{b_1}} & \boldsymbol{b}_{\boldsymbol{b_2}} & \boldsymbol{b}_{\boldsymbol{b_3}} & \boldsymbol{b}_{\boldsymbol{b_4}} \end{bmatrix} \boldsymbol{f}_{\boldsymbol{p}}, \tag{20}
$$

with

$$
\boldsymbol{b}_{\boldsymbol{a_i}} = \begin{bmatrix} s_{\alpha_i} \\ 0 \\ c_{\alpha_i} \end{bmatrix}, \quad \boldsymbol{b}_{\boldsymbol{b_i}} = \begin{bmatrix} d_{\mathfrak{C}_{i_y}}^{\mathfrak{B}} c_{\alpha_i} + k\lambda_i s_{\alpha_1} \\ d_{\mathfrak{C}_{i_z}}^{\mathfrak{B}} s_{\alpha_i} - d_{\mathfrak{C}_{i_x}}^{\mathfrak{B}} c_{\alpha_i} \\ -d_{\mathfrak{C}_{i_y}}^{\mathfrak{B}} s_{\alpha_i} - k c_{\alpha_i} \end{bmatrix},
$$

for $i = 1,\ 2,\ 3,\ 4$, and with $k = \frac{k_\tau}{k_e}$, $\lambda_1 = \lambda_3 = -1$ and $\lambda_2 = \lambda_4 = 1$.
With the relations (19) and (20), we write the vector $\boldsymbol{f}(\boldsymbol{q})$ as

$$
\boldsymbol{f}(\boldsymbol{q}) = \begin{bmatrix}
\boldsymbol{R}_{\mathfrak{B}}^{\mathfrak{I}} \boldsymbol{B}_{\boldsymbol{a}} & \mathbb{O}_{3\times6} \\
\boldsymbol{W}_{\boldsymbol{\eta}}^T \boldsymbol{B}_{\boldsymbol{b}} & \mathbb{O}_{3\times6} \\
\mathbb{O}_{6\times4} & \mathbb{I}_{6\times6}
\end{bmatrix} \begin{bmatrix} \boldsymbol{f}_{\boldsymbol{p}} \\ \boldsymbol{\tau}_{\boldsymbol{\alpha}} \\ \boldsymbol{\tau}_{\boldsymbol{\gamma}} \end{bmatrix} = \boldsymbol{B}(\boldsymbol{q}) \boldsymbol{u}, \tag{21}
$$

with $\boldsymbol{B_a} = \begin{bmatrix} \boldsymbol{b_{a_1}} & \boldsymbol{b_{a_2}} & \boldsymbol{b_{a_3}} & \boldsymbol{b_{a_4}} \end{bmatrix}$, $\boldsymbol{B_b} = \begin{bmatrix} \boldsymbol{b_{b_1}} & \boldsymbol{b_{b_2}} & \boldsymbol{b_{b_3}} & \boldsymbol{b_{b_4}} \end{bmatrix}$, and where $\boldsymbol{u} \in \mathbb{R}^{10\times 1}$ is the real input control.
In conclusion, we use the model developed in this section to emulate a real H-shaped quad tilt rotor equipped with a camera in numerical simulations.

2.3 Simplified Dynamic Model for Control Design

As we are dealing with a strong and complex system, we simplify the complete model obtained in Section 2.2 to facilitate the control system development.
In this section, the main objective is to obtain a decoupled dynamic model. For that, we write the model as a sum of a decoupled dynamics and the errors due to the coupling terms neglected, just like

$$\boldsymbol{M}(\boldsymbol{q}) = \hat{\boldsymbol{M}}(\boldsymbol{q}) + \tilde{\boldsymbol{M}}(\boldsymbol{q}), \tag{22}$$
$$\boldsymbol{C}(\boldsymbol{q},\dot{\boldsymbol{q}}) = \hat{\boldsymbol{C}}(\boldsymbol{q},\boldsymbol{q}) + \tilde{\boldsymbol{C}}(\boldsymbol{q},\dot{\boldsymbol{q}}), \tag{23}$$
$$\boldsymbol{g}(\boldsymbol{q}) = \hat{\boldsymbol{g}}(\boldsymbol{q}) + \tilde{\boldsymbol{g}}(\boldsymbol{q}), \tag{24}$$

where $\hat{\boldsymbol{M}}(\boldsymbol{q})$, $\hat{\boldsymbol{C}}(\boldsymbol{q},\dot{\boldsymbol{q}})$, and $\hat{\boldsymbol{g}}(\boldsymbol{q})$ are the decoupled model and $\tilde{\boldsymbol{M}}(\boldsymbol{q})$, $\tilde{\boldsymbol{C}}(\boldsymbol{q},\dot{\boldsymbol{q}})$, and $\tilde{\boldsymbol{g}}(\boldsymbol{q})$ are the errors. With those matrices and vectors, we rewrite the model (12) as

$$\ddot{\boldsymbol{q}} = \hat{\boldsymbol{M}}^{-1}(\boldsymbol{q})\left(-\hat{\boldsymbol{C}}(\boldsymbol{q},\dot{\boldsymbol{q}})\dot{\boldsymbol{q}} - \hat{\boldsymbol{g}}(\boldsymbol{q}) + \boldsymbol{f}(\boldsymbol{q})\right) + \boldsymbol{\rho}(\boldsymbol{q},\dot{\boldsymbol{q}},\ddot{\boldsymbol{q}}), \tag{25}$$

with

$$\boldsymbol{\rho}(\boldsymbol{q},\dot{\boldsymbol{q}},\ddot{\boldsymbol{q}}) = \hat{\boldsymbol{M}}^{-1}(\boldsymbol{q})\left(\boldsymbol{f_d} - \tilde{\boldsymbol{M}}(\boldsymbol{q})\ddot{\boldsymbol{q}} - \tilde{\boldsymbol{C}}(\boldsymbol{q},\dot{\boldsymbol{q}}) - \tilde{\boldsymbol{g}}(\boldsymbol{q})\right) + \boldsymbol{d}(t), \tag{26}$$

where the vector $\boldsymbol{d}(t) \in \mathbb{R}^{12\times 1}$ is added to represent wind gusts disturbances.
Note that $\boldsymbol{\rho}(\boldsymbol{q},\dot{\boldsymbol{q}},\ddot{\boldsymbol{q}})$ depends of the generalized coordinates and its time derivatives. As those coordinates are bounded, it is reasonable to make the following assumption.

Assumption 1 *The uncertainty $\boldsymbol{\rho}(\boldsymbol{q},\dot{\boldsymbol{q}},\ddot{\boldsymbol{q}})$ is bounded as*

$$\|\boldsymbol{\rho}(\boldsymbol{q},\dot{\boldsymbol{q}},\ddot{\boldsymbol{q}})\| \leq \bar{\boldsymbol{\rho}}, \tag{27}$$

with $\bar{\boldsymbol{\rho}} \geq 0$.

In addition, we can obtain a decoupled vector $\bar{\boldsymbol{\rho}} = \begin{bmatrix} \bar{\boldsymbol{\rho}}_{\boldsymbol{\xi}}^T & \bar{\boldsymbol{\rho}}_{\boldsymbol{\eta}}^T & \bar{\boldsymbol{\rho}}_{\boldsymbol{\alpha}}^T & \bar{\boldsymbol{\rho}}_{\boldsymbol{\gamma}}^T \end{bmatrix}^T$ through numerical simulation considering the generalized coordinates boundaries.
In the following, we omit the terms $(\boldsymbol{q})$, $(\boldsymbol{q},\dot{\boldsymbol{q}})$, $(\boldsymbol{q},\dot{\boldsymbol{q}},\ddot{\boldsymbol{q}})$ and (t) to simplify the notation.
To obtain a decoupled system, we consider: i) the origin of $\mathfrak{B}$, $\mathfrak{C}_0$ and $\mathfrak{C}_5$ are coincident, which imply in $\boldsymbol{d}_{\mathfrak{C}_0}^{\mathfrak{B}} = \boldsymbol{d}_{\mathfrak{C}_5}^{\mathfrak{B}} = \mathbb{O}_{3\times 1}$; ii) the rotors are symmetrically located, which lead to $|d_{\mathfrak{C}_{ix}}^{\mathfrak{B}}| = \bar{d}_x$, $|d_{\mathfrak{C}_{iy}}^{\mathfrak{B}}| = \bar{d}_y$ and $|d_{\mathfrak{C}_{iz}}^{\mathfrak{B}}| = 0$, for $i = 1,\ 2,\ 3,\ 4$; iii) the dynamics of the UAV attitude and rotors inclination are decoupled, by doing $\boldsymbol{J}_{\mathfrak{B}_0} \gg \boldsymbol{J}_{\mathfrak{B}_i} \approx \mathbb{O}_{3\times 3}$, for $i = 1,\ 2,\ 3,\ 4,\ 5$; iv) the mass and inertia of the rotors are equal; and v) the coupling terms are $\boldsymbol{M}_{\boldsymbol{\eta},\boldsymbol{\alpha}} \approx \mathbb{O}_{3\times 4}$ and $\boldsymbol{M}_{\boldsymbol{\eta},\boldsymbol{\gamma}} \approx \mathbb{O}_{3\times 2}$. By doing this, we obtain

$$\hat{\boldsymbol{M}} = \begin{bmatrix} \hat{\boldsymbol{M}}_{\boldsymbol{\xi}} & \mathbb{O}_{3\times 3} & \mathbb{O}_{3\times 4} & \mathbb{O}_{3\times 2} \\ \mathbb{O}_{3\times 3} & \hat{\boldsymbol{M}}_{\boldsymbol{\eta}} & \mathbb{O}_{3\times 4} & \mathbb{O}_{3\times 2} \\ \mathbb{O}_{4\times 3} & \mathbb{O}_{4\times 3} & \hat{\boldsymbol{M}}_{\boldsymbol{\alpha}} & \mathbb{O}_{4\times 2} \\ \mathbb{O}_{2\times 3} & \mathbb{O}_{2\times 3} & \mathbb{O}_{2\times 4} & \hat{\boldsymbol{M}}_{\boldsymbol{\gamma}} \end{bmatrix}, \quad \hat{\boldsymbol{C}} = \begin{bmatrix} \mathbb{O}_{3\times 3} & \mathbb{O}_{3\times 3} & \mathbb{O}_{3\times 4} & \mathbb{O}_{3\times 2} \\ \mathbb{O}_{3\times 3} & \hat{\boldsymbol{C}}_{\boldsymbol{\eta}} & \mathbb{O}_{3\times 4} & \mathbb{O}_{3\times 2} \\ \mathbb{O}_{4\times 3} & \mathbb{O}_{4\times 3} & \mathbb{O}_{4\times 4} & \mathbb{O}_{4\times 2} \\ \mathbb{O}_{2\times 3} & \mathbb{O}_{2\times 3} & \mathbb{O}_{2\times 4} & \hat{\boldsymbol{C}}_{\boldsymbol{\gamma}} \end{bmatrix}, \quad \hat{\boldsymbol{g}} = \begin{bmatrix} \hat{\boldsymbol{g}}_{\boldsymbol{\xi}} \\ \mathbb{O}_{3\times 1} \\ \mathbb{O}_{4\times 1} \\ \mathbb{O}_{2\times 1} \end{bmatrix}.$$

We also have coupling terms in the vector $\boldsymbol{f}(\boldsymbol{q})$, as we can see in (21). Thus, to divide the dynamics (25), we consider the relations (19) and (20) and obtain

$$\ddot{\boldsymbol{\xi}} = \hat{\boldsymbol{M}}_{\boldsymbol{\xi}}^{-1}\left(-\hat{\boldsymbol{G}}_{\boldsymbol{\xi}} + \boldsymbol{R}_{\mathfrak{B}}^{\mathfrak{I}} f^{\mathfrak{B}}\right) + \boldsymbol{\rho}_{\boldsymbol{\xi}}, \tag{28}$$

$$\ddot{\boldsymbol{\eta}} = \hat{\boldsymbol{M}}_{\boldsymbol{\eta}}^{-1}\left(-\hat{\boldsymbol{C}}_{\boldsymbol{\eta}}\dot{\boldsymbol{\eta}} + \boldsymbol{W}_{\boldsymbol{\eta}}^{T}\boldsymbol{\tau}^{\mathfrak{B}}\right) + \boldsymbol{\rho}_{\boldsymbol{\eta}}, \tag{29}$$

$$\ddot{\boldsymbol{\alpha}} = \hat{\boldsymbol{M}}_{\boldsymbol{\alpha}}^{-1}\boldsymbol{\tau}_{\boldsymbol{\alpha}} + \boldsymbol{\rho}_{\boldsymbol{\alpha}}, \tag{30}$$

$$\ddot{\boldsymbol{\gamma}} = \hat{\boldsymbol{M}}_{\boldsymbol{\gamma}}^{-1}\left(-\hat{\boldsymbol{C}}_{\boldsymbol{\gamma}}\dot{\boldsymbol{\gamma}} + \boldsymbol{\tau}_{\boldsymbol{\alpha}}\right) + \boldsymbol{\rho}_{\boldsymbol{\gamma}}. \tag{31}$$

Finally, we use the subsystems (28), (29), (30) and (31) for the control system development.

3. Control

This section develops a robust control system for the H-shaped quad tilt rotor equipped with a camera. We observe in Section 2.3that we are dealing with a nonlinear and underactuated system. A common solution found in the literature corresponds to developing a cascade control system to deal with the underactuated behavior. In this scheme, we control the UAV position in the outer loop and the UAV attitude in the inner loop and use the roll reference as an intermediate control input.
As we can see in (28) and (29), the control input are the signals $f^{\mathfrak{B}}$ and $\boldsymbol{\tau}^{\mathfrak{B}}$. To obtain the propellers forces and rotors inclination correspondent to the force and torque in $\mathfrak{B}$, we develop a mapping basing on the work of [20]. The control scheme proposed is presented in Figure (3).

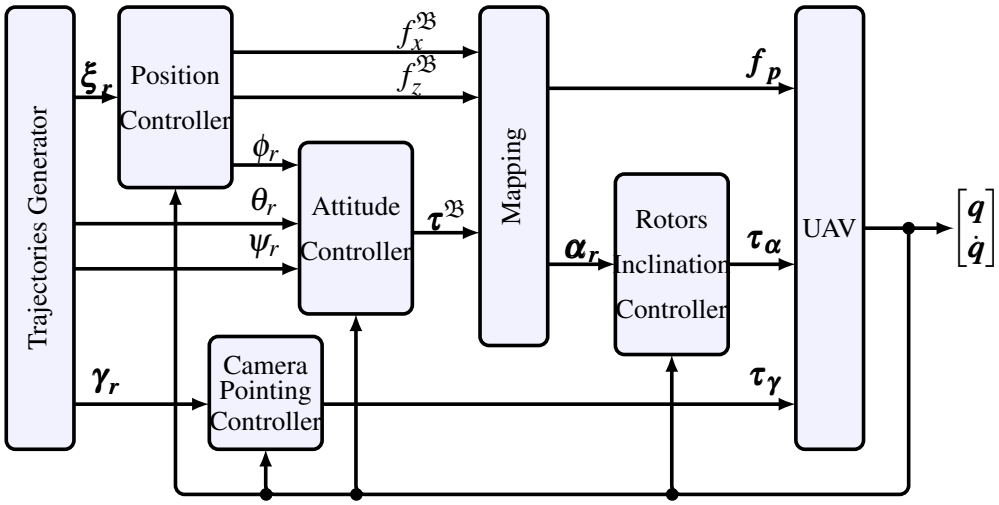

Figure 3 – Control Scheme.

To control the UAV position, we choose the feedback linearization and the robust control H_∞ techniques. We use the generalized super-twisting sliding mode control technique with a control law to compensate for the nonlinearities for the remaining subsystems.

3.1 UAV Position Controller

In this section, we develop the control system for the UAV position using the feedback linearization and the robust control H_∞ techniques.
Considering the dynamic (28), which will be used for the control development, we formulate the feedback linearization control law as

$$f^{\mathfrak{B}} = \left(\boldsymbol{R}_{\mathfrak{B}}^{\mathfrak{I}}\right)^{T}\left(\hat{\boldsymbol{M}}_{\boldsymbol{\xi}}^{-1}\left(\boldsymbol{v}_{\boldsymbol{\xi}} + \ddot{\boldsymbol{\xi}}_{\boldsymbol{r}}\right) + \hat{\boldsymbol{G}}_{\boldsymbol{\xi}}\right), \tag{32}$$

where $\boldsymbol{\xi}_{\boldsymbol{r}} = \begin{bmatrix} x_r & y_r & z_r \end{bmatrix}^T$ is the position reference and $\boldsymbol{v}_{\boldsymbol{\xi}} = \begin{bmatrix} v_x & v_y & v_z \end{bmatrix}^T$ is the control law formulated by the robust H_∞ technique. Replacing the control law in (28) and being $\tilde{\boldsymbol{\xi}} = \boldsymbol{\xi} - \boldsymbol{\xi}_{\boldsymbol{r}}$ the error dynamics,

we obtain the following linear and decoupled dynamics

$$\ddot{\tilde{\boldsymbol{\xi}}} = \boldsymbol{v_\xi} + \boldsymbol{\rho_\xi}. \tag{33}$$

As we are dealing with a decoupled dynamic, we divide (33) in the three subsystems $\ddot{x} = v_x + \rho_x$, $\ddot{y} = v_y + \rho_y$ and $\ddot{z} = v_z + \rho_z$. To write a state space model, we define as states vector $\tilde{\boldsymbol{q}}_{\boldsymbol{x}} = \begin{bmatrix}\tilde{x} & \dot{\tilde{x}} & \int\tilde{x}\end{bmatrix}^T$, $\tilde{\boldsymbol{q}}_{\boldsymbol{y}} = \begin{bmatrix}\tilde{y} & \dot{\tilde{y}} & \int\tilde{y}\end{bmatrix}^T$, and $\tilde{\boldsymbol{q}}_{\boldsymbol{z}} = \begin{bmatrix}\tilde{z} & \dot{\tilde{z}} & \int\tilde{z}\end{bmatrix}^T$, where the integral term is added to improve the system response. With those vectors, we write each dynamic as

$$\dot{\tilde{\boldsymbol{q}}}_{\boldsymbol{i}} = \boldsymbol{A_i}\tilde{\boldsymbol{q}}_{\boldsymbol{i}} + \boldsymbol{b_{u_i}}v_i + \boldsymbol{b_{d_i}}\boldsymbol{\rho_i}, \tag{34}$$

with

$$\boldsymbol{A_i} = \begin{bmatrix}0 & 1 & 0\\ 0 & 0 & 0\\ 1 & 0 & 0\end{bmatrix}, \quad \boldsymbol{b_{u_i}} = \begin{bmatrix}0\\1\\0\end{bmatrix}, \quad \boldsymbol{b_{d_i}} = \begin{bmatrix}0\\1\\0\end{bmatrix}, \tag{35}$$

for $i = \{x,\ y,\ z\}$.
We design the control laws as $v_i = \boldsymbol{k_i}\tilde{\boldsymbol{q}}_{\boldsymbol{i}}$, where $\boldsymbol{k_i} \in \mathbb{R}^{1\times 3}$, for $i = \{x,\ y,\ z\}$, are gains vectors. Replacing those control laws and being $\boldsymbol{\vartheta_i}$ the output system for input $\boldsymbol{\rho_i}$, we have in closed-loop

$$\begin{aligned}\dot{\boldsymbol{q}}_{\boldsymbol{i}} &= \underbrace{(\boldsymbol{A_i} + \boldsymbol{b_{u_i}}\boldsymbol{k_i})}_{\boldsymbol{A_{cl_i}}}\tilde{\boldsymbol{q}}_{\boldsymbol{i}} + \boldsymbol{b_{d_i}}\boldsymbol{\rho_i} \quad = \boldsymbol{A_{cl_i}}\tilde{\boldsymbol{q}}_{\boldsymbol{i}} + \boldsymbol{b_{d_i}}\boldsymbol{\rho_i}\\ \boldsymbol{\vartheta_i} &= \underbrace{(\boldsymbol{C_i} + \boldsymbol{d_{u_i}}\boldsymbol{k_i})}_{\boldsymbol{C_{cl_i}}}\tilde{\boldsymbol{q}}_{\boldsymbol{i}} + \boldsymbol{d_{d_i}}\boldsymbol{\rho_i} \quad = \boldsymbol{C_{cl_i}}\tilde{\boldsymbol{q}}_{\boldsymbol{i}} + \boldsymbol{d_{d_i}}\boldsymbol{\rho_i},\end{aligned} \tag{36}$$

where $\boldsymbol{C_i}$, $\boldsymbol{d_{u_i}}$, and $\boldsymbol{d_{d_i}}$, for $i = \{x,\ y,\ z\}$, are weighting matrices for the robust control H_∞.
The objective of the robust H_∞ control technique is to minimize the system norm H_∞, minimizing the disturbance effect on the system output [23, 24]. Being $H_i(s)$ the system transfer function and considering the disturbances $\boldsymbol{\rho_i}$ have energy bounded, we can write

$$\|H_i(s)\|_\infty = sup\frac{\|\boldsymbol{\vartheta_i}\|_2}{\|\boldsymbol{\rho_i}\|_2} \leq \chi_i, \tag{37}$$

for $i = \{x,\ y,\ z\}$.
To analyze the closed loop stability, we propose the Lyapunov function $V(\tilde{\boldsymbol{q}}_{\boldsymbol{i}}) = \tilde{\boldsymbol{q}}_{\boldsymbol{i}}^T\boldsymbol{P_i}\tilde{\boldsymbol{q}}_{\boldsymbol{i}}$, $\boldsymbol{P_i} = \boldsymbol{P_i}^T > 0$, whose derivative $\dot{V}_i(\tilde{\boldsymbol{q}}_{\boldsymbol{i}})$ must be negative definite. Considering (37) and $\dot{V}_i(\tilde{\boldsymbol{q}}_{\boldsymbol{i}}) = \dot{\tilde{\boldsymbol{q}}}_{\boldsymbol{i}}^T\boldsymbol{P_i}\tilde{\boldsymbol{q}}_{\boldsymbol{i}} + \tilde{\boldsymbol{q}}_{\boldsymbol{i}}^T\boldsymbol{P_i}\dot{\tilde{\boldsymbol{q}}}_{\boldsymbol{i}} < 0$, we write

$$\dot{\tilde{\boldsymbol{q}}}_{\boldsymbol{i}}^T\boldsymbol{P_i}\tilde{\boldsymbol{q}}_{\boldsymbol{i}} + \tilde{\boldsymbol{q}}_{\boldsymbol{i}}^T\boldsymbol{P_i}\dot{\tilde{\boldsymbol{q}}}_{\boldsymbol{i}} + \boldsymbol{\vartheta}_{\boldsymbol{i}}^T\boldsymbol{\vartheta_i} - \chi_i^2\boldsymbol{\rho}_{\boldsymbol{i}}^T\boldsymbol{\rho_i} < 0, \tag{38}$$

for $i = \{x,\ y,\ z\}$.
With the dynamic (36), we rewrite (38) as

$$\begin{bmatrix}\tilde{\boldsymbol{q}}_{\boldsymbol{i}}^T & \boldsymbol{\rho}_{\boldsymbol{i}}^T\end{bmatrix}\begin{bmatrix}\boldsymbol{A_{cl_i}}^T\boldsymbol{P_i} + \boldsymbol{P_i}\boldsymbol{A_{cl_i}} + \boldsymbol{C_{cl_i}}^T\boldsymbol{C_{cl_i}} & \boldsymbol{P_i}\boldsymbol{B_{d_i}} + \boldsymbol{C_{cl_i}}^T\boldsymbol{D_{d_i}}\\ \boldsymbol{B_{d_i}}^T\boldsymbol{P_i} + \boldsymbol{D_{d_i}}^T\boldsymbol{C_{cl_i}} & \boldsymbol{D_{d_i}}^T\boldsymbol{D_{d_i}} - \chi^2\mathbb{I}\end{bmatrix}\begin{bmatrix}\tilde{\boldsymbol{q}}_{\boldsymbol{i}}\\ \boldsymbol{\rho_i}\end{bmatrix} < 0, \tag{39}$$

for $i = \{x,\ y,\ z\}$. We verify that (39) is negative definite if the following condition is satisfied

$$\begin{bmatrix}\boldsymbol{A_{cl_i}}^T\boldsymbol{P_i} + \boldsymbol{P_i}\boldsymbol{A_{cl_i}} + \boldsymbol{C_{cl_i}}^T\boldsymbol{C_{cl_i}} & \boldsymbol{P_i}\boldsymbol{B_{d_i}} + \boldsymbol{C_{cl_i}}^T\boldsymbol{D_{d_i}}\\ \boldsymbol{B_{d_i}}^T\boldsymbol{P_i} + \boldsymbol{D_{d_i}}^T\boldsymbol{C_{cl_i}} & \boldsymbol{D_{d_i}}^T\boldsymbol{D_{d_i}} - \chi^2\mathbb{I}\end{bmatrix} < 0, \tag{40}$$

for $i = \{x,\ y,\ z\}$. To formulate a stabilization problem, we manipulate mathematically the matrix in (40) to become it linear. The mathematical manipulation consist in the following steps: i) pre and post multiply the matrix by diag $(\boldsymbol{P_i}^{-1}, \mathbb{I})$; ii) apply the Schur complement [23]; and iii) change the variables $\boldsymbol{W_i} = \boldsymbol{P_i}^{-1}$, $\boldsymbol{Y_i} = \boldsymbol{k_i}\boldsymbol{P_i}^{-1}$, $\mu_i = \chi_i^2$. Then, we obtain

$$\begin{bmatrix}\boldsymbol{A_i}\boldsymbol{W_i} + \boldsymbol{W_i}\boldsymbol{A_i}^T + \boldsymbol{B_{u_i}}\boldsymbol{Y_i} + \boldsymbol{Y_i}^T\boldsymbol{B_{u_i}} & * & *\\ \boldsymbol{B_{d_i}} & -\mu_i\mathbb{I} & *\\ \boldsymbol{C_i}\boldsymbol{W_i} + \boldsymbol{D_{u_i}}\boldsymbol{Y_i} & \boldsymbol{D_{d_i}} & \mathbb{I}\end{bmatrix} < 0, \tag{41}$$

for $i = \{x,\ y,\ z\}$.
Considering (41), we propose the Theorem 1 in order to minimize the $\|H_i\|_\infty$.

Theorem 1 *Characterizing the norm of the closed-loop system (36) as $\|H_i\|_\infty \leq \chi_i$, if the following optimization problem*

$$\begin{aligned}
&\underset{\mu,\ \boldsymbol{W_i},\ \boldsymbol{Y_i}}{\textit{minimize}} \quad \mu_i \\
&\textit{subject to} \\
&\boldsymbol{Y_i} > 0, && (42)\\
&\boldsymbol{W_i} = \boldsymbol{W_i}^T > 0, && (43)\\
&\begin{bmatrix} \boldsymbol{A_i W_i} + \boldsymbol{W_i A_i}^T + \boldsymbol{B_{u_i} Y_i} + \boldsymbol{Y_i}^T \boldsymbol{B_{u_i}} & * & * \\ \boldsymbol{B_{d_i}} & -\mu_i \mathbb{I} & * \\ \boldsymbol{C_i W_i} + \boldsymbol{D_{u_i} Y_i} & \boldsymbol{D_{d_i}} & \mathbb{I} \end{bmatrix} < 0 && (44)
\end{aligned}$$

is feasible, the closed-loop system (36) is asymptotically stable and the gains matrices and the norm H_∞ are given by

$$\boldsymbol{k_i} = \boldsymbol{Y_i W_i}^{-1}, \tag{45}$$
$$\|H_i\|_\infty \leq \sqrt{\mu_i}, \tag{46}$$

for $i = \{x,\ y,\ z\}$.

3.2 UAV Attitude, Rotors Inclination and Camera Pointing Controllers

We design the UAV attitude, rotors inclinations and camera pointing controllers basing on the dynamics (29), (30) and (31). First, we divide the control signals $\boldsymbol{\tau}^{\mathfrak{B}}$, $\boldsymbol{\tau_\alpha}$ and $\boldsymbol{\tau_\gamma}$ as

$$\boldsymbol{\tau}^{\mathfrak{B}} = \hat{\boldsymbol{\tau}}^{\mathfrak{B}} + \boldsymbol{\tau}_{\mathbf{1}}^{\mathfrak{B}}, \tag{47}$$
$$\boldsymbol{\tau_\alpha} = \hat{\boldsymbol{\tau}}_{\boldsymbol{\alpha}} + \boldsymbol{\tau}_{\mathbf{1}_{\boldsymbol{\alpha}}}, \tag{48}$$
$$\boldsymbol{\tau_\gamma} = \hat{\boldsymbol{\tau}}_{\boldsymbol{\gamma}} + \boldsymbol{\tau}_{\mathbf{1}_{\boldsymbol{\gamma}}}, \tag{49}$$

where $\hat{\boldsymbol{\tau}}^{\mathfrak{B}} = \begin{bmatrix} \hat{\tau}_\phi^{\mathfrak{B}} & \hat{\tau}_\theta^{\mathfrak{B}} & \hat{\tau}_\psi^{\mathfrak{B}} \end{bmatrix}^T$, $\hat{\boldsymbol{\tau}}_{\boldsymbol{\alpha}} = \begin{bmatrix} \hat{\tau}_{\alpha_1} & \hat{\tau}_{\alpha_2} & \hat{\tau}_{\alpha_3} & \hat{\tau}_{\alpha_4} \end{bmatrix}^T$ and $\hat{\boldsymbol{\tau}}_{\boldsymbol{\gamma}} = \begin{bmatrix} \hat{\tau}_{\gamma_1} & \hat{\tau}_{\gamma_2} \end{bmatrix}^T$ are responsible to compensate the nonlinearities and to stabilize the nominal system, and $\boldsymbol{\tau}_{\mathbf{1}}^{\mathfrak{B}} = \begin{bmatrix} \tau_{1_\phi}^{\mathfrak{B}} & \tau_{1_\theta}^{\mathfrak{B}} & \tau_{1_\psi}^{\mathfrak{B}} \end{bmatrix}^T$, $\boldsymbol{\tau}_{\mathbf{1}_{\boldsymbol{\alpha}}} = \begin{bmatrix} \tau_{1_{\alpha_1}} & \tau_{1_{\alpha_2}} & \tau_{1_{\alpha_3}} & \tau_{1_{\alpha_4}} \end{bmatrix}^T$ and $\boldsymbol{\tau}_{\mathbf{1}_{\boldsymbol{\gamma}}} = \begin{bmatrix} \tau_{1_{\gamma_1}} & \tau_{1_{\gamma_2}} \end{bmatrix}^T$ are formulated to deal with the external disturbances and modeling errors, adding robustness to the system.
We develop the control system in three steps: i) sliding surface synthesis; ii) formulation of the control laws $\hat{\boldsymbol{\tau}}^{\mathfrak{B}}$, $\hat{\boldsymbol{\tau}}_{\boldsymbol{\alpha}}$ and $\hat{\boldsymbol{\tau}}_{\boldsymbol{\gamma}}$; and iii) formulation of the control laws $\boldsymbol{\tau}_{\mathbf{1}}^{\mathfrak{B}}$, $\boldsymbol{\tau}_{\mathbf{1}_{\boldsymbol{\alpha}}}$ and $\boldsymbol{\tau}_{\mathbf{1}_{\boldsymbol{\gamma}}}$.
The usual choice of the sliding surfaces is a linear combination of the system states errors. Being the error dynamic $\tilde{\boldsymbol{\eta}} = \boldsymbol{\eta} - \boldsymbol{\eta_r}$, $\tilde{\boldsymbol{\alpha}} = \boldsymbol{\alpha} - \boldsymbol{\alpha_r}$ and $\tilde{\boldsymbol{\gamma}} = \boldsymbol{\gamma} - \boldsymbol{\gamma_r}$, where $\boldsymbol{\eta_r}$, $\boldsymbol{\alpha_r}$ and $\boldsymbol{\gamma_r}$ are the desire references, we define as states vector $\tilde{\boldsymbol{q}}_{\boldsymbol{\eta}} = \begin{bmatrix} \tilde{\boldsymbol{\eta}}^T & \dot{\boldsymbol{\eta}}^T & \int \tilde{\boldsymbol{\eta}}^T \end{bmatrix}^T$, $\tilde{\boldsymbol{q}}_{\boldsymbol{\alpha}} = \begin{bmatrix} \tilde{\boldsymbol{\alpha}}^T & \dot{\boldsymbol{\alpha}}^T & \int \tilde{\boldsymbol{\alpha}}^T \end{bmatrix}^T$ and $\tilde{\boldsymbol{q}}_{\boldsymbol{\gamma}} = \begin{bmatrix} \tilde{\boldsymbol{\gamma}}^T & \dot{\boldsymbol{\gamma}}^T & \int \tilde{\boldsymbol{\gamma}}^T \end{bmatrix}^T$.
We add the integral term to improve the system response. With those vectors, we define the sliding surfaces as

$$\boldsymbol{\sigma_\eta} = \dot{\tilde{\boldsymbol{\eta}}} + \boldsymbol{\Lambda_{1_\eta}} \tilde{\boldsymbol{\eta}} + \boldsymbol{\Lambda_{2_\eta}} \int_0^t \tilde{\boldsymbol{\eta}} d\tau, \tag{50}$$
$$\boldsymbol{\sigma_\alpha} = \dot{\tilde{\boldsymbol{\alpha}}} + \boldsymbol{\Lambda_{1_\alpha}} \tilde{\boldsymbol{\alpha}} + \boldsymbol{\Lambda_{2_\alpha}} \int_0^t \tilde{\boldsymbol{\alpha}} d\tau, \tag{51}$$
$$\boldsymbol{\sigma_\gamma} = \dot{\tilde{\boldsymbol{\gamma}}} + \boldsymbol{\Lambda_{1_\gamma}} \tilde{\boldsymbol{\gamma}} + \boldsymbol{\Lambda_{2_\gamma}} \int_0^t \tilde{\boldsymbol{\gamma}} d\tau, \tag{52}$$

where $\boldsymbol{\sigma_\eta} = \begin{bmatrix}\sigma_\phi & \sigma_\theta & \sigma_\psi\end{bmatrix}^T$, $\boldsymbol{\sigma_\alpha} = \begin{bmatrix}\sigma_{\alpha_1} & \sigma_{\alpha_2} & \sigma_{\alpha_3} & \sigma_{\alpha_4}\end{bmatrix}^T$ and $\boldsymbol{\sigma_\gamma} = \begin{bmatrix}\sigma_{\gamma_1} & \sigma_{\gamma_2}\end{bmatrix}^T$ are the sliding surfaces and

$$\boldsymbol{\Lambda_{1_\eta}} = \text{diag}\left(\lambda_{\phi_1}, \lambda_{\theta_1}, \lambda_{\psi_1}\right) \in \mathbb{R}^{3\times3}, \quad \boldsymbol{\Lambda_{1_\alpha}} = \text{diag}\left(\lambda_{\alpha_{11}}, \lambda_{\alpha_{21}}, \lambda_{\alpha_{31}}, \lambda_{\alpha_{41}}\right) \in \mathbb{R}^{4\times4}, \boldsymbol{\Lambda_{1_\gamma}} = \text{diag}\left(\lambda_{\gamma_{11}}, \lambda_{\gamma_{21}}\right) \in \mathbb{R}^{2\times2},$$
$$\boldsymbol{\Lambda_{2_\eta}} = \text{diag}\left(\lambda_{\phi_2}, \lambda_{\theta_2}, \lambda_{\psi_2}\right) \in \mathbb{R}^{3\times3}, \quad \boldsymbol{\Lambda_{2_\alpha}} = \text{diag}\left(\lambda_{\alpha_{12}}, \lambda_{\alpha_{22}}, \lambda_{\alpha_{32}}, \lambda_{\alpha_{42}}\right) \in \mathbb{R}^{4\times4}, \boldsymbol{\Lambda_{2_\gamma}} = \text{diag}\left(\lambda_{\gamma_{12}}, \lambda_{\gamma_{22}}\right) \in \mathbb{R}^{2\times2},$$

are gains defined by the designer.
We formulate the control laws $\hat{\boldsymbol{\tau}}_{\boldsymbol{\eta}}$, $\hat{\boldsymbol{\tau}}_{\boldsymbol{\alpha}}$ and $\hat{\boldsymbol{\tau}}_{\boldsymbol{\gamma}}$ as

$$\hat{\boldsymbol{\tau}}^{\mathfrak{B}} = \boldsymbol{W_\eta}\left(\hat{\boldsymbol{M}}_{\boldsymbol{\eta}}\boldsymbol{\nu_\eta} + \hat{\boldsymbol{C}}_{\boldsymbol{\eta}}\dot{\boldsymbol{\eta}}\right), \tag{53}$$
$$\hat{\boldsymbol{\tau}}_{\boldsymbol{\alpha}} = \hat{\boldsymbol{M}}_{\boldsymbol{\alpha}}\boldsymbol{\nu_\alpha}, \tag{54}$$
$$\hat{\boldsymbol{\tau}}_{\boldsymbol{\gamma}} = \left(\hat{\boldsymbol{M}}_{\boldsymbol{\gamma}}\boldsymbol{\nu_\gamma} + \hat{\boldsymbol{C}}_{\boldsymbol{\gamma}}\dot{\boldsymbol{\gamma}}\right), \tag{55}$$

with

$$\boldsymbol{\nu_\eta} = \ddot{\boldsymbol{\eta}}_{\boldsymbol{r}} - \boldsymbol{\Lambda_{1_\eta}}\dot{\tilde{\boldsymbol{\eta}}} - \boldsymbol{\Lambda_{2_\eta}}\tilde{\boldsymbol{\eta}},$$
$$\boldsymbol{\nu_\alpha} = \ddot{\boldsymbol{\alpha}}_{\boldsymbol{r}} - \boldsymbol{\Lambda_{1_\alpha}}\dot{\tilde{\boldsymbol{\alpha}}} - \boldsymbol{\Lambda_{2_\alpha}}\tilde{\boldsymbol{\alpha}},$$
$$\boldsymbol{\nu_\gamma} = \ddot{\boldsymbol{\gamma}}_{\boldsymbol{r}} - \boldsymbol{\Lambda_{1_\gamma}}\dot{\tilde{\boldsymbol{\gamma}}} - \boldsymbol{\Lambda_{2_\gamma}}\tilde{\boldsymbol{\gamma}}.$$

We formulate the control laws $\boldsymbol{\tau}_{\mathbf{1}}^{\mathfrak{B}}$, $\boldsymbol{\tau_{1_\alpha}}$ and $\boldsymbol{\tau_\gamma}$ as

$$\boldsymbol{\tau}_{\mathbf{1}}^{\mathfrak{B}} = \boldsymbol{W_\eta}\hat{\boldsymbol{M}}_{\boldsymbol{\eta}}\boldsymbol{\tau}_{\boldsymbol{gst}}^{\mathfrak{B}}, \tag{56}$$
$$\boldsymbol{\tau_{1_\alpha}} = \hat{\boldsymbol{M}}_{\boldsymbol{\alpha}}\boldsymbol{\tau}_{\boldsymbol{gst_\alpha}}, \tag{57}$$
$$\boldsymbol{\tau_{1_\gamma}} = \hat{\boldsymbol{M}}_{\boldsymbol{\gamma}}\boldsymbol{\tau}_{\boldsymbol{gst_\gamma}}, \tag{58}$$

where $\boldsymbol{\tau}_{gst}^{\mathfrak{B}} = \begin{bmatrix}\tau_{gst_\phi}^{\mathfrak{B}} & \tau_{gst_\theta}^{\mathfrak{B}} & \tau_{gst_\psi}^{\mathfrak{B}}\end{bmatrix}^T$, $\boldsymbol{\tau}_{gst_\alpha} = \begin{bmatrix}\tau_{gst_{\alpha_1}} & \tau_{gst_{\alpha_2}} & \tau_{gst_{\alpha_3}} & \tau_{gst_{\alpha_4}}\end{bmatrix}^T$ and $\boldsymbol{\tau}_{gst_\gamma} = \begin{bmatrix}\tau_{gst_{\gamma_1}} & \tau_{gst_{\gamma_2}}\end{bmatrix}^T$ are formulated using the generalized super-twisting technique just like

$$\boldsymbol{\tau}_{\boldsymbol{gst}}^{\mathfrak{B}} = -\boldsymbol{K_{1_\eta}}\boldsymbol{\nu_{1_\eta}} - \boldsymbol{K_{2_\eta}}\int_0^t \boldsymbol{\nu_{2_\eta}}d\tau, \tag{59}$$
$$\boldsymbol{\tau}_{\boldsymbol{gst_\alpha}} = -\boldsymbol{K_{1_\alpha}}\boldsymbol{\nu_{1_\alpha}} - \boldsymbol{K_{2_\alpha}}\int_0^t \boldsymbol{\nu_{2_\alpha}}d\tau, \tag{60}$$
$$\boldsymbol{\tau}_{\boldsymbol{gst_\gamma}} = -\boldsymbol{K_{1_\gamma}}\boldsymbol{\nu_{1_\gamma}} - \boldsymbol{K_{2_\gamma}}\int_0^t \boldsymbol{\nu_{2_\gamma}}d\tau, \tag{61}$$

where $\boldsymbol{\nu_{1_\eta}} = \begin{bmatrix}\nu_{i_\phi} & \nu_{i_\theta} & \nu_{i_\psi}\end{bmatrix}^T$, $\boldsymbol{\nu_{i_\alpha}} = \begin{bmatrix}\nu_{i_{\alpha_1}} & \nu_{i_{\alpha_2}} & \nu_{i_{\alpha_3}} & \nu_{i_{\alpha_4}}\end{bmatrix}^T$ and $\boldsymbol{\nu_{i_\gamma}} = \begin{bmatrix}\nu_{i_{\gamma_1}} & \nu_{i_{\gamma_2}}\end{bmatrix}^T$, for $i = 1,\ 2$, are equal to

$$\begin{array}{rcl}\boldsymbol{\nu_{1_i}} & = & |\boldsymbol{\sigma_i}|^{\frac{1}{2}}sign(\boldsymbol{\sigma_i}) + \boldsymbol{k_{3_i}}\boldsymbol{\sigma_i}, \\ \boldsymbol{\nu_{2_i}} & = & \frac{1}{2}sign(\boldsymbol{\sigma_i}) + \frac{3}{2}\boldsymbol{k_{3_i}}|\boldsymbol{\sigma_i}|^{\frac{1}{2}}sign(\boldsymbol{\sigma_i}) + \boldsymbol{k_{3_i}^2}\boldsymbol{\sigma_i},\end{array} \tag{62}$$

for $i = \{\boldsymbol{\eta},\ \boldsymbol{\alpha},\ \boldsymbol{\gamma}\}$, with

$$\boldsymbol{K_{1_\eta}} = \text{diag}\left(k_{1_\phi}, k_{1_\theta}, k_{1_\psi}\right) \in \mathbb{R}^{3\times3}, \quad \boldsymbol{K_{1_\alpha}} = \text{diag}\left(k_{1_{\alpha_1}}, k_{1_{\alpha_2}}, k_{1_{\alpha_3}}, k_{1_{\alpha_4}}\right) \in \mathbb{R}^{4\times4}, \boldsymbol{K_{1_\gamma}} = \text{diag}\left(k_{1_{\gamma_1}}, k_{1_{\gamma_2}}\right) \in \mathbb{R}^{2\times2},$$
$$\boldsymbol{K_{2_\eta}} = \text{diag}\left(k_{2_\phi}, k_{2_\theta}, k_{2_\psi}\right) \in \mathbb{R}^{3\times3}, \quad \boldsymbol{K_{2_\alpha}} = \text{diag}\left(k_{2_{\alpha_1}}, k_{2_{\alpha_2}}, k_{2_{\alpha_3}}, k_{2_{\alpha_4}}\right) \in \mathbb{R}^{4\times4}, \boldsymbol{K_{2_\gamma}} = \text{diag}\left(k_{2_{\gamma_1}}, k_{2_{\gamma_2}}\right) \in \mathbb{R}^{2\times2},$$
$$\boldsymbol{K_{3_\eta}} = \text{diag}\left(k_{3_\phi}, k_{3_\theta}, k_{3_\psi}\right) \in \mathbb{R}^{3\times3}, \quad \boldsymbol{K_{3_\alpha}} = \text{diag}\left(k_{3_{\alpha_1}}, k_{3_{\alpha_2}}, k_{3_{\alpha_3}}, k_{3_{\alpha_4}}\right) \in \mathbb{R}^{4\times4}, \boldsymbol{K_{3_\gamma}} = \text{diag}\left(k_{3_{\gamma_1}}, k_{3_{\gamma_2}}\right) \in \mathbb{R}^{2\times2}.$$

being gains defined by the designer.
Applying the control laws (53) and (56) in (29), (54) and (57) in (30), and (55) and (58) in (31), we have in closed-loop

$$\dot{\boldsymbol{\sigma}}_{\boldsymbol{\eta}}(\boldsymbol{q},\dot{\boldsymbol{q}},\ddot{\boldsymbol{q}}) = -\boldsymbol{K}_{\mathbf{1}_{\boldsymbol{\eta}}}\boldsymbol{\nu}_{\mathbf{1}_{\boldsymbol{\eta}}} - \boldsymbol{K}_{\mathbf{2}_{\boldsymbol{\eta}}}\int_0^t \boldsymbol{\nu}_{\mathbf{2}_{\boldsymbol{\eta}}} d\tau + \boldsymbol{\rho}_{\boldsymbol{\eta}}, \tag{63}$$

$$\dot{\boldsymbol{\sigma}}_{\boldsymbol{\alpha}}(\boldsymbol{q},\dot{\boldsymbol{q}},\ddot{\boldsymbol{q}}) = -\boldsymbol{K}_{\mathbf{1}_{\boldsymbol{\alpha}}}\boldsymbol{\nu}_{\mathbf{1}_{\boldsymbol{\alpha}}} - \boldsymbol{K}_{\mathbf{2}_{\boldsymbol{\alpha}}}\int_0^t \boldsymbol{\nu}_{\mathbf{2}_{\boldsymbol{\alpha}}} d\tau + \boldsymbol{\rho}_{\boldsymbol{\alpha}}, \tag{64}$$

$$\dot{\boldsymbol{\sigma}}_{\boldsymbol{\gamma}}(\boldsymbol{q},\dot{\boldsymbol{q}},\ddot{\boldsymbol{q}}) = -\boldsymbol{K}_{\mathbf{1}_{\boldsymbol{\gamma}}}\boldsymbol{\nu}_{\mathbf{1}_{\boldsymbol{\gamma}}} - \boldsymbol{K}_{\mathbf{2}_{\boldsymbol{\gamma}}}\int_0^t \boldsymbol{\nu}_{\mathbf{2}_{\boldsymbol{\gamma}}} d\tau + \boldsymbol{\rho}_{\boldsymbol{\gamma}}. \tag{65}$$

Defining the new variables $\boldsymbol{h_i} = \begin{bmatrix} h_{1_i} & h_{2_i} \end{bmatrix}^T = \begin{bmatrix} \sigma_i & k_{2_i}\int_0^t \nu_{2_i} d\tau + \rho_i \end{bmatrix}^T$, we rewrite the dynamics (63), (64) and (65) in a scalar way just like

$$\begin{array}{rcl} \dot{h}_{1_i} & = & -k_{1_i}\nu_{1_i} + h_{2_i} \\ \dot{h}_{2_i} & = & -k_{2_i}\nu_{2_i} + \dot{\rho}_i, \end{array} \tag{66}$$

for $i = \{\phi,\ \theta,\ \psi,\ \alpha_1,\ \alpha_2,\ \alpha_3,\ \alpha_4,\ \gamma_1,\ \gamma_2\}$.

Assumption 2 *The uncertainty $\dot{\rho}_i(\boldsymbol{q},\dot{\boldsymbol{q}},\ddot{\boldsymbol{q}})$ is limited as*

$$|\dot{\rho}_i(\boldsymbol{q},\dot{\boldsymbol{q}},\ddot{\boldsymbol{q}})| \leq \bar{\bar{\rho}}_i, \tag{67}$$

with $\bar{\bar{\rho}}_i \geq 0$, for $i = \{\phi,\ \theta,\ \psi,\ \alpha_1,\ \alpha_2,\ \alpha_3,\ \alpha_4,\ \gamma_1,\ \gamma_2\}$.

To verify the conditions in which the system trajectories converge to the sliding surfaces, we realize the following procedure basing in the work of [19, 25].
To verify the system convergence in finite time, the authors in 19 define the vector $\boldsymbol{\zeta} = \begin{bmatrix} \nu_{1_i} & h_{2_i} \end{bmatrix}^T$, whose dynamic is written as

$$\dot{\boldsymbol{\zeta}}_{\boldsymbol{i}} = \begin{bmatrix} \dot{\zeta}_{1_i} \\ \dot{\zeta}_{2_i} \end{bmatrix} = \nu'_{1_i} \underbrace{\begin{bmatrix} -k_{1_i} & 1 \\ -k_{2_i} + \tilde{\rho}_i & \end{bmatrix}}_{\boldsymbol{A_i}} \begin{bmatrix} \zeta_{1_i} \\ \zeta_{2_i} \end{bmatrix} = \nu'_{1_i}\boldsymbol{A_i}\boldsymbol{\zeta_i}, \tag{68}$$

with

$$\nu'_{1_i} = \frac{\nu_{2_i}}{\nu_{1_i}} = \frac{1}{2|h_{1_i}|^{\frac{1}{2}}} + k_{3_i}, \quad \tilde{\rho}_i = \frac{1}{\nu_{2_i}}\dot{\rho}_i,$$

for $i = \{\phi,\ \theta,\ \psi,\ \alpha_1,\ \alpha_2,\ \alpha_3,\ \alpha_4,\ \gamma_1,\ \gamma_2\}$. Note that if $\boldsymbol{\zeta_i}$ converges in finite time to origin, then, $\boldsymbol{h_i}$ also converges, for $i = \{\phi,\ \theta,\ \psi,\ \alpha_1,\ \alpha_2,\ \alpha_3,\ \alpha_4,\ \gamma_1,\ \gamma_2\}$, [25].

Assumption 3 *The uncertainty $\tilde{\rho}_i(\boldsymbol{q},\dot{\boldsymbol{q}},\ddot{\boldsymbol{q}})$ is limited as*

$$|\tilde{\rho}_i(\boldsymbol{q},\dot{\boldsymbol{q}},\ddot{\boldsymbol{q}})| \leq \left|\frac{\dot{\rho}_i}{\nu_{2_i}}\right| \leq 2\bar{\bar{\rho}}_i, \tag{69}$$

with $\bar{\bar{\rho}}_i \geq 0$, for $i = \{\phi,\ \theta,\ \psi,\ \alpha_1,\ \alpha_2,\ \alpha_3,\ \alpha_4,\ \gamma_1,\ \gamma_2\}$.

Using $\boldsymbol{\zeta_i}$, 19 proposed the quadratic Lyapunov function $V_i(\boldsymbol{\zeta_i}) = \boldsymbol{\zeta_i}^T\boldsymbol{P_i}\boldsymbol{\zeta_i}$, with $\boldsymbol{P_i} = \boldsymbol{P_i}^T > 0$, for $i = \{\phi,\ \theta,\ \psi,\ \alpha_1,\ \alpha_2,\ \alpha_3,\ \alpha_4,\ \gamma_1,\ \gamma_2\}$. Basing in [25], the authors chose the following matrix $\boldsymbol{P_i}$

$$\boldsymbol{P_i} = \begin{bmatrix} p_{1_i} + p_{2_i}^2 & -p_{2_i} \\ -p_{2_i} & 1 \end{bmatrix}, \tag{70}$$

with $p_{1_i} > 0$, for $i = \{\phi,\ \theta,\ \psi,\ \alpha_1,\ \alpha_2,\ \alpha_3,\ \alpha_4,\ \gamma_1,\ \gamma_2\}$.

Deriving $V_i(\boldsymbol{\zeta_i})$, we obtain

$$\dot{V}_i(\boldsymbol{\zeta}) = \nu'_{1_i}\boldsymbol{\zeta_i}^T\left(\boldsymbol{A_i}^T\boldsymbol{P_i}+\boldsymbol{P_i}\boldsymbol{A_i}\right)\boldsymbol{\zeta_i}, \tag{71}$$

for $i = \{\phi,\ \theta,\ \psi,\ \alpha_1,\ \alpha_2,\ \alpha_3,\ \alpha_4,\ \gamma_1,\ \gamma_2\}$. Considering Assumption 3, we rewrite (71) as

$$\dot{V}_i(\boldsymbol{\zeta}) \leq -\nu'_{1_i}\boldsymbol{\zeta_i}^T\boldsymbol{Q_i}\boldsymbol{\zeta_i}, \tag{72}$$

where $\boldsymbol{Q_i} = -\left(\boldsymbol{A_i}^T\boldsymbol{P_i}+\boldsymbol{P_i}\boldsymbol{A_i}\right)$, with

$$\boldsymbol{Q_i} = \begin{bmatrix} 2k_{1_i}(p_{1_i}+p_{2_i}^2)-2p_{2_i}(2\bar{\rho}_i+k_{2_i}) & -p_{2_i}^2-k_{1_i}p_{2_i}+k_{2_i}-p_{1_i}+2\bar{\rho}_i \\ -p_{2_i}^2-k_{1_i}p_{2_i}+k_{2_i}-p_{1_i}+2\bar{\rho}_i & 2p_{2_i} \end{bmatrix}, \tag{73}$$

for $i = \{\phi,\ \theta,\ \psi,\ \alpha_1,\ \alpha_2,\ \alpha_3,\ \alpha_4,\ \gamma_1,\ \gamma_2\}$. We can observe that $\dot{V}_i(\boldsymbol{\zeta_i})$ in (71) is negative definite if $\boldsymbol{Q_i}$ is positive definite. To verify the positiveness of $\boldsymbol{Q_i}$, first we choose $k_{2_i} = k_{1_i}p_{2_i}+p_{1_i}$ and then we check the conditions in what $\boldsymbol{Q_i}$ is positive definite. From then on, we propose the Theorem 2.

Theorem 2 *The trajectories of the closed-loop systems (63), (64) and (65) converge in finite time to the sliding surfaces if the following conditions are satisfied*

$$p_{1_i} > 0, \tag{74}$$
$$p_{2_i} > 0, \tag{75}$$
$$k_{1_i} > \frac{4p_{1_i}p_{2_i}^2+\left(2\bar{\rho}_i+p_{2_i}^2\right)^2}{4p_{1_i}p_{2_i}}, \tag{76}$$
$$k_{2_i} = k_{1_i}p_{2_i}+p_{1_i}, \tag{77}$$
$$k_{3_i} > 0, \tag{78}$$

for $i = \{\phi,\ \theta,\ \psi,\ \alpha_1,\ \alpha_2,\ \alpha_3,\ \alpha_4,\ \gamma_1,\ \gamma_2\}$.

3.3 Mapping

This section develops the mapping proposed to obtain the propellers forces and rotors inclination correspondent to the signals generated from the UAV position and attitude controllers exist in $\mathfrak{B}$. The mapping presented in this work is based in [20].
We rewrite the relations in (19) and (20) as

$$\mathfrak{f} = \mathscr{B}\bar{\boldsymbol{f}}_{\boldsymbol{p}}, \tag{79}$$

with

$$\mathfrak{f} = \begin{bmatrix} f_x^{\mathfrak{B}} \\ f_z^{\mathfrak{B}} \\ \tau_\phi^{\mathfrak{B}} \\ \tau_\theta^{\mathfrak{B}} \\ \tau_\psi^{\mathfrak{B}} \end{bmatrix}, \quad \bar{\boldsymbol{f}}_{\boldsymbol{p}} = \begin{bmatrix} f_{p_{x_1}} \\ f_{p_{z_1}} \\ f_{p_{x_2}} \\ f_{p_{x_2}} \\ f_{p_{x_3}} \\ f_{p_{z_3}} \\ f_{p_{x_4}} \\ f_{p_{z_4}} \end{bmatrix}, \quad \mathscr{B} = \begin{bmatrix} 1 & 0 & 1 & 0 & 1 & 0 & 1 & 0 \\ 0 & 1 & 0 & 1 & 0 & 1 & 0 & 1 \\ -k & -\bar{d}_y & k & \bar{d}_y & -k & \bar{d}_y & k & -\bar{d}_y \\ 0 & \bar{d}_x & 0 & \bar{d}_x & 0 & -\bar{d}_x & 0 & -\bar{d}_x \\ \bar{d}_y & -k & -\bar{d}_y & k & -\bar{d}_y & -k & \bar{d}_y & k \end{bmatrix},$$

where $f_{p_{x_i}} = f_{p_i}s_{\alpha_i}$ and $f_{p_{z_i}} = f_{p_i}c_{\alpha_i}$, for $i = 1,\ 2,\ 3,\ 4$, are the component of the propellers forces in ${}^{\mathfrak{B}}x$ and ${}^{\mathfrak{B}}z$ directions, respectively.
As $\mathscr{B}$ is not square, we use the pseudo-inverse matrix of Moore-Penrose $\mathscr{B}^\dagger$, obtaining the following inverse relation

$$\bar{\boldsymbol{f}}_{\boldsymbol{p}} = \mathscr{B}^\dagger\mathfrak{f}. \tag{80}$$

Table 1 – UAV parameters.

Parameter	Value	Parameter	Value
m_0	$1.5\ kg$	$\boldsymbol{d}_{\mathfrak{C}_0}^{\mathfrak{B}}$	$\begin{bmatrix}0 & 0 & -0.05\end{bmatrix}^T\ m$
m_1,m_2,m_3,m_4	$0.15\ kg$	$\boldsymbol{d}_{\mathfrak{C}_1}^{\mathfrak{B}}$	$\begin{bmatrix}-0.35 & -0.35 & 0\end{bmatrix}^T\ m$
m_5	$0.15\ kg$	$\boldsymbol{d}_{\mathfrak{C}_2}^{\mathfrak{B}}$	$\begin{bmatrix}-0.35 & 0.35 & 0\end{bmatrix}^T\ m$
$\boldsymbol{I}_{\mathfrak{C}_0}$	diag $(36.3, 36.3, 61.5) \times 10^{-3} kgm^2$	$\boldsymbol{d}_{\mathfrak{C}_3}^{\mathfrak{B}}$	$\begin{bmatrix}0.35 & 0.35 & 0\end{bmatrix}^T\ m$
$\boldsymbol{I}_{\mathfrak{C}_1}$,$\boldsymbol{I}_{\mathfrak{C}_2}$,$\boldsymbol{I}_{\mathfrak{C}_3}$,$\boldsymbol{I}_{\mathfrak{C}_4}$	diag $(8, 7, 2) \times 10^{-5} kgm^2$	$\boldsymbol{d}_{\mathfrak{C}_4}^{\mathfrak{B}}$	$\begin{bmatrix}0.35 & -0.35 & 0\end{bmatrix}^T\ m$
$\boldsymbol{I}_{\mathfrak{C}_5}$	diag $(2, 2, 2) \times 10^{-5} kgm^2$	$\boldsymbol{d}_{\mathfrak{C}_5}^{\mathfrak{B}}$	$\begin{bmatrix}0 & 0 & -0.1\end{bmatrix}^T\ m$
k_τ	$1.7 \times 10^{-7}\ Nms^2$		
k_e	$9.5 \times 10^{-6}\ Ns^2$		
g	$9.81\ ms^{-2}$		

From (80), we calculate the propellers forces and the rotors inclination references as

$$f_{p_i} = \sqrt{f_{p_{x_i}}^2 + f_{p_{z_i}}^2}$$
$$\alpha_{r_i} = atan2\left(f_{p_{x_i}}, f_{p_{z_i}}\right),$$

para $i = 1,\ 2,\ 3,\ 4$.

4. Results

In this section, we present the results obtained from numerical simulations realized in MATLAB/Simulink software.

In the simulation, we use the complete model developed in Section 2.2 The parameters used are presented in Table 1, which were obtained from the previous work [20, 21].

To simulate a situation closer to the real, we add disturbances to represent aerodynamic external forces and wind gusts. The forces with magnitude $2N$, $2N$ and $-2N$ were applied in the forces $f_x^{\mathfrak{I}}$, $f_y^{\mathfrak{I}}$ and $f_z^{\mathfrak{I}}$ at $10s$, $25s$ and $40s$ respectively. To represent wind gusts, we applied the disturbance $d_i(t) = 0.2sin(0.2t)m/s^2$, for $i = \{x,\ y,\ z\}$, and $d_i(t) = 0.2sin(0.2t)rad/s^2$, for $i = \{\phi,\ \theta,\ \psi,\ \alpha_1,\ \alpha_2,\ \alpha_3,\ \alpha_4,\ \gamma_1,\ \gamma_2\}$. We also considered saturating actuators, with which the forces and torques can vary between $0N \leq f_{p_1}, f_{p_2}, f_{p_3}, f_{p_4} \leq 18N$ and $-1N.m \leq \tau_{\alpha_1}, \tau_{\alpha_2}, \tau_{\alpha_3}, \tau_{\alpha_4}, \tau_{\gamma_1}, \tau_{\gamma_2} \leq 1N.m$.

To obtain the UAV position controller gains, we chose the weighting matrices $\boldsymbol{C_i}$, $\boldsymbol{d_{u_i}}$ and $\boldsymbol{d_{d_i}}$, for $i = \{x,\ y,\ z\}$, according to the settling time, control effort and action of the disturbance in the system output, respectively. Then, we resolved the optimization problem presented in Theorem 1. After some analysis of the system output, we chose the values presented in Table 2.

We choose the gains of the UAV attitude, rotors inclination and camera pointing controllers according to the conditions in (74), (75), (76), (77) and (78). To estimate a boundary for the disturbances $\boldsymbol{\rho_\eta}$, $\boldsymbol{\rho_\alpha}$ and $\boldsymbol{\rho_\gamma}$, we make some numerical analysis, and we verified that is reasonable to adopt the values presented in Table 3. Additionally, we verified that the greater the gain k_{1_i}, the faster the system response. Concerning to k_{2_i}, we note that it affects the system robustness, i.e., the greater the gain k_{2_i}, the more robust the system response. Finally, we chose p_{1_i}, p_{2_i} and k_{3_i}, obtained the gains k_{1_i} and k_{2_i} and tested in numerical simulations until the system response was satisfactory, for $i = \{\phi,\ \theta,\ \psi,\ \alpha_1,\ \alpha_2,\ \alpha_3,\ \alpha_4,\ \gamma_1,\ \gamma_2\}$. We present the gains chosen in Table 3, where $\boldsymbol{p_{i_\eta}} = \begin{bmatrix}p_{i_\phi} & p_{i_\theta} & p_{i_\psi}\end{bmatrix}$, $\boldsymbol{p_{i_\alpha}} = \begin{bmatrix}p_{i_{\alpha_1}} & p_{i_{\alpha_2}} & p_{i_{\alpha_3}} & p_{i_{\alpha_4}}\end{bmatrix}$ and $\boldsymbol{p_{i_\alpha}} = \begin{bmatrix}p_{i_{\gamma_1}} & p_{i_{\gamma_2}}\end{bmatrix}$, for $i = 1,\ 2$.

In order to have variations of the generalized coordinates and its time derivatives, the desired trajectory consists of an 8-shaped curve with an initial path beginning on the floor. Without this path, in the beginning, the altitude error is high, demanding a strong control effort. Thus, the UAV starts executing the trajectory on the floor and, when it reaches the desired altitude, it starts to execute the 8-shaped curve, which has the following structure

Table 2 – Robust H_∞ Control: Parameters and Gains.

	Parameter	Value	Gain	Value
x	$\boldsymbol{C_x}$	$\text{diag}(3, 1.5, 3)$		
	$\boldsymbol{d_{u_x}}$	$\begin{bmatrix}0 & 0.1 & 0.1\end{bmatrix}^T$	$\boldsymbol{k_x}$	$\begin{bmatrix}-23.7272 & -8.6238 & -34.9940\end{bmatrix}$
	$\boldsymbol{d_{d_x}}$	$\begin{bmatrix}0 & 0.4 & 1\end{bmatrix}^T$		
y	$\boldsymbol{C_y}$	$\text{diag}(2, 1, 2)$		
	$\boldsymbol{d_{u_y}}$	$\begin{bmatrix}0 & 0.1 & 0.1\end{bmatrix}^T$	$\boldsymbol{k_y}$	$\begin{bmatrix}-19.1286 & -6.7548 & -26.2795\end{bmatrix}$
	$\boldsymbol{d_{d_y}}$	$\begin{bmatrix}0 & 0.3 & 1\end{bmatrix}^T$		
z	$\boldsymbol{C_z}$	$\text{diag}(4, 1, 4)$		
	$\boldsymbol{d_{u_z}}$	$\begin{bmatrix}0 & 0.1 & 0.1\end{bmatrix}^T$	$\boldsymbol{k_z}$	$\begin{bmatrix}-29.3486 & -8.1534 & -48.5580\end{bmatrix}$
	$\boldsymbol{d_{d_z}}$	$\begin{bmatrix}0 & 0.4 & 1\end{bmatrix}^T$		

Table 3 – GSTA: Parameters and Gains.

	Parameter	Value	Gain	Value
$\boldsymbol{\eta}$	$\boldsymbol{p_{1_\eta}}$	$\begin{bmatrix}2 & 1.4 & 2\end{bmatrix}$	$\boldsymbol{K_{1_\eta}}$	$\text{diag}(8.4391, 7.7344, 10.7667)$
			$\boldsymbol{K_{2_\eta}}$	$\text{diag}(2.3442, 2.9748, 2.6917)$
	$\boldsymbol{p_{2_\eta}}$	$\begin{bmatrix}1.8 & 1.3 & 2\end{bmatrix}$	$\boldsymbol{K_{3_\eta}}$	$\text{diag}(1, 1, 1)$
			$\boldsymbol{\Lambda_{1_\eta}}$	$\text{diag}(10, 6, 10)$
	$\bar{\bar{\boldsymbol{\rho}}}_{\boldsymbol{\eta}}$	$\begin{bmatrix}2 & 2 & 2\end{bmatrix}^T$	$\boldsymbol{\Lambda_{2_\eta}}$	$\text{diag}(25, 9, 25)$
$\boldsymbol{\alpha}$	$\boldsymbol{p_{1_\alpha}}$	$\begin{bmatrix}2 & 2 & 2 & 2\end{bmatrix}$	$\boldsymbol{K_{1_\alpha}}$	$\text{diag}(8.4391, 8.4391, 8.4391, 8.4391)$
			$\boldsymbol{K_{2_\alpha}}$	$\text{diag}(2.3442, 2.3442, 2.3442, 2.3442)$
	$\boldsymbol{p_{2_\alpha}}$	$\begin{bmatrix}1.8 & 1.8 & 1.8 & 1.8\end{bmatrix}$	$\boldsymbol{K_{3_\alpha}}$	$\text{diag}(1, 1, 1, 1)$
			$\boldsymbol{\Lambda_{1_\alpha}}$	$\text{diag}(40, 40, 40, 40)$
	$\bar{\bar{\boldsymbol{\rho}}}_{\boldsymbol{\alpha}}$	$\begin{bmatrix}2 & 2 & 2 & 2\end{bmatrix}^T$	$\boldsymbol{\Lambda_{2_\alpha}}$	$\text{diag}(400, 400, 400, 400)$
$\boldsymbol{\gamma}$	$\boldsymbol{p_{1_\gamma}}$	$\begin{bmatrix}2 & 2\end{bmatrix}$	$\boldsymbol{K_{1_\gamma}}$	$\text{diag}(10.7667, 10.7667)$
			$\boldsymbol{K_{2_\gamma}}$	$\text{diag}(2.6917, 2.6917)$
	$\boldsymbol{p_{2_\gamma}}$	$\begin{bmatrix}2 & 2\end{bmatrix}$	$\boldsymbol{K_{3_\gamma}}$	$\text{diag}(1, 1)$
			$\boldsymbol{\Lambda_{1_\gamma}}$	$\text{diag}(40, 40)$
	$\bar{\bar{\boldsymbol{\rho}}}_{\boldsymbol{\gamma}}$	$\begin{bmatrix}2 & 2\end{bmatrix}^T$	$\boldsymbol{\Lambda_{2_\gamma}}$	$\text{diag}(400, 400)$

$$x = 5cos\left(\frac{\pi}{22}t\right), \tag{81}$$

$$y = 5sin\left(\frac{\pi}{11}t\right), \tag{82}$$

$$z = 6 - 6e^{-t}. \tag{83}$$

We chose a trajectory that varies between a sinusoidal curve and a constant path to see variations of the gimbal coordinates for the gimbal.

In Figure 4, we present the UAV trajectory desired and executed. We see the UAV was capable of the trajectory imposed for it. More specifically, in Figure 5a, we present the generalized coordinates of the UAV position and its tracking errors. We observe the trajectory tracking with errors during the simulation. The error at $5s$, approximately, occurred when the UAV reached the desired altitude due to the direction's change. At $10s$, in $\tilde{x}$ graph, at $25s$, in $\tilde{y}$ graph, and at $40s$, in $\tilde{z}$ graph it is possible to observe the effect of the disturbances on the generalized forces that are rejected by the control system.

In Figure 5b, we present the generalized coordinates that represent the UAV attitude, their tracking errors, and their respectively sliding surface. In the graph of the roll angle, we see that the trajectory tracking. In the error graphs, we see variations in the beginning and at $25s$. The first one occurred because the system did not reach the sliding surface yet. The last one is addressed to the disturbance

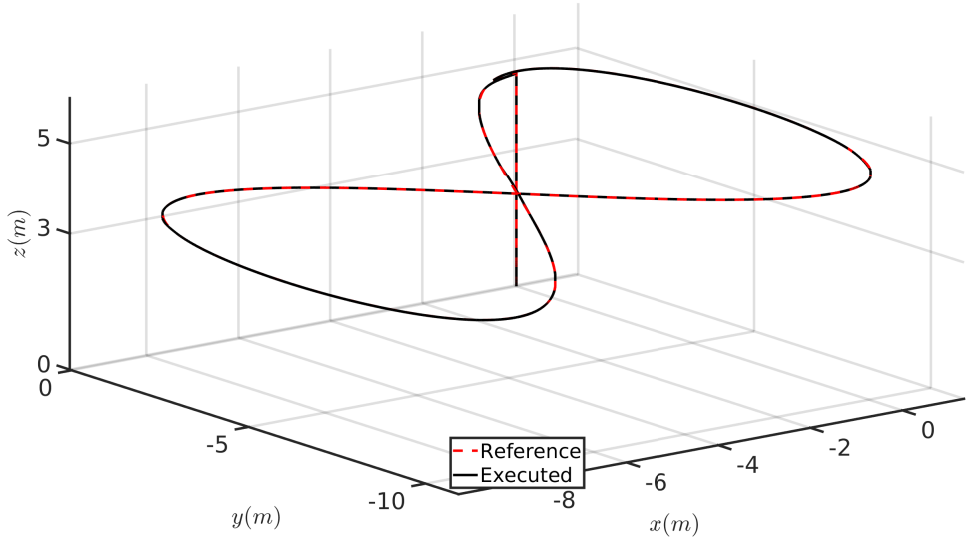

Figure 4 – UAV trajectory.

applied in $f_y^{\mathfrak{I}}$, since the UAV had to move in ${}^{\mathfrak{B}}y$ direction to compensate the disturbance. Also, we see almost no variation of the pitch angle, even the UAV moving in ${}^{\mathfrak{B}}x$ direction.
In Figure 5c, we present the rotors' angle inclination, their tracking errors, and their sliding surfaces. We observe the rotors inclined to UAV move in ${}^{\mathfrak{B}}x$ direction. We note oscillations, which came from the UAV attitude controller, but with low amplitudes. We also see the effect of the disturbance $f_y^{\mathfrak{I}}$ at $25s$.
Concerning the gimbal movement, we see in Figure 5d tracking errors in the changes of the path, i.e., when they change from the constant path to the sinusoidal path and vice-versa. More specifically, in the γ_1 graph, we see a higher variation due to the initial conditions errors.
In Figure 6a, the propellers' forces reached the upper limit of the saturator, but in the rest of the simulation, they kept within the boundaries. Regarding the rotors' torque, in Figure 6b, we see they within the saturators limits and with small variations due to the chattering. In Figure 6c, we also that the torques of the gimbal kept within the saturation boundaries, and they also have small amplitudes.

5. Conclusion

In Figure 5b, we present the generalized coordinates that represent the UAV attitude, their tracking errors, and their respectively sliding surface. In the graph of the roll angle, we see that the trajectory tracking. In the error graphs, we see variations in the beginning and at $25s$. The first one occurred because the system did not reach the sliding surface yet. The last one is addressed to the disturbance applied in $f_y^{\mathfrak{I}}$, since the UAV had to move in ${}^{\mathfrak{B}}y$ direction to compensate the disturbance. Also, we see almost no variation of the pitch angle, even the UAV moving in ${}^{\mathfrak{B}}x$ direction.
This work presented the mathematical modeling of an H-shaped quad tilt rotor equipped with a camera. We developed a control system to track feasible trajectories and orientate the camera. We formulated a complete dynamic model to emulate a real UAV in numerical simulations and a simplified dynamic model to facilitate the control system design. To control the UAV position, we used the robust H_∞ and the feedback linearization control techniques. For the UAV attitude, rotors inclination, and camera pointing controllers, we used the GSTA and compensation of the nonlinearities. To verify the control system proposed, we performed simulations with the complete dynamic model, and we verified that the system showed a satisfactory response since it reached the desired objective. We concluded that the strategy adopted is conservative since we consider the worst case of perturbations. For future works, we propose to use adaptive control laws to obtain a less conservative strategy.

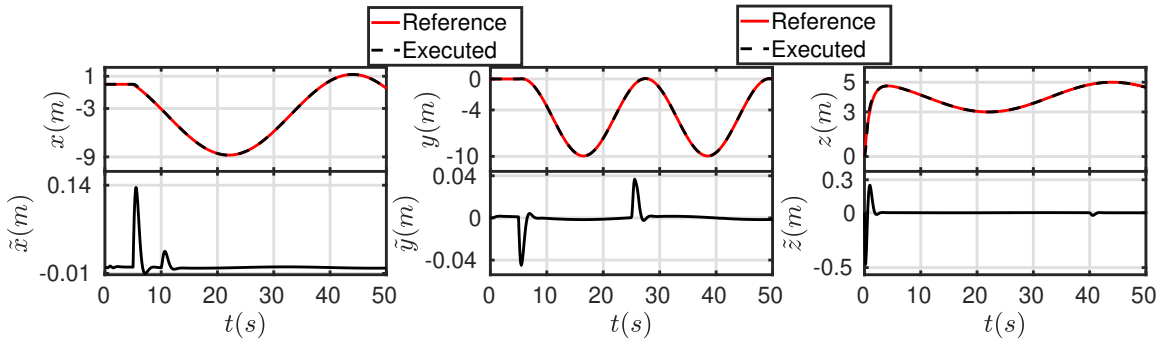

(a) UAV position and tracking errors.

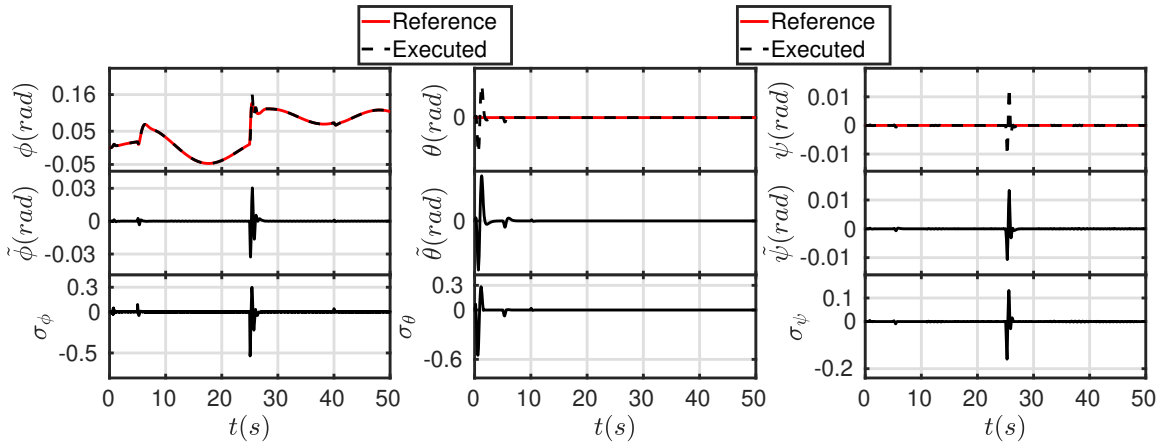

(b) UAV attitude, tracking errors and sliding surfaces.

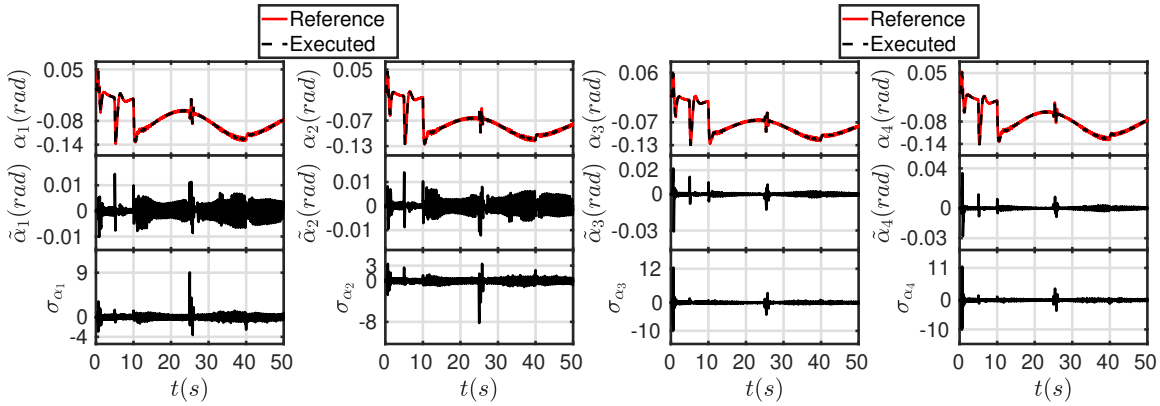

(c) Rotors inclination, tracking errors and sliding surfaces.

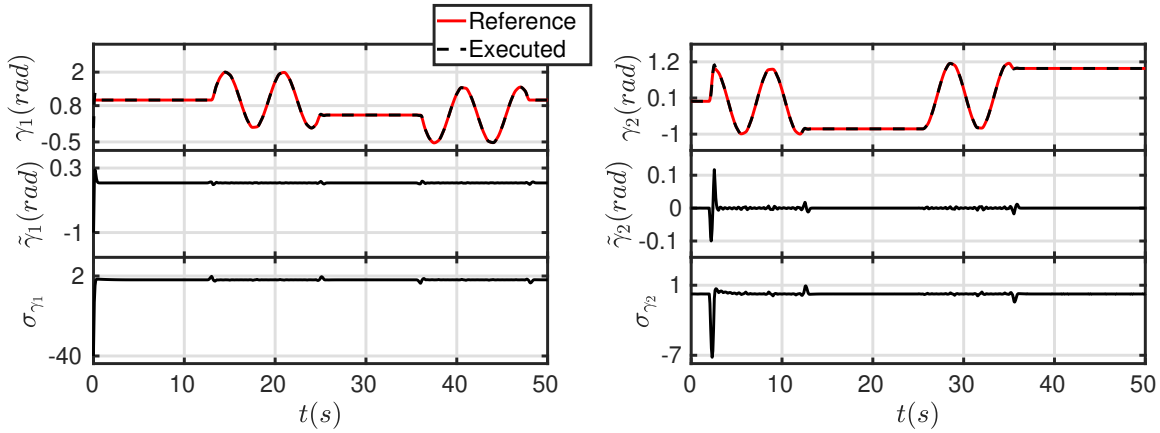

(d) Camera pointing, tracking errors and sliding surfaces.

Figure 5 – Generalized coordinates, tracking errors and sliding surfaces.

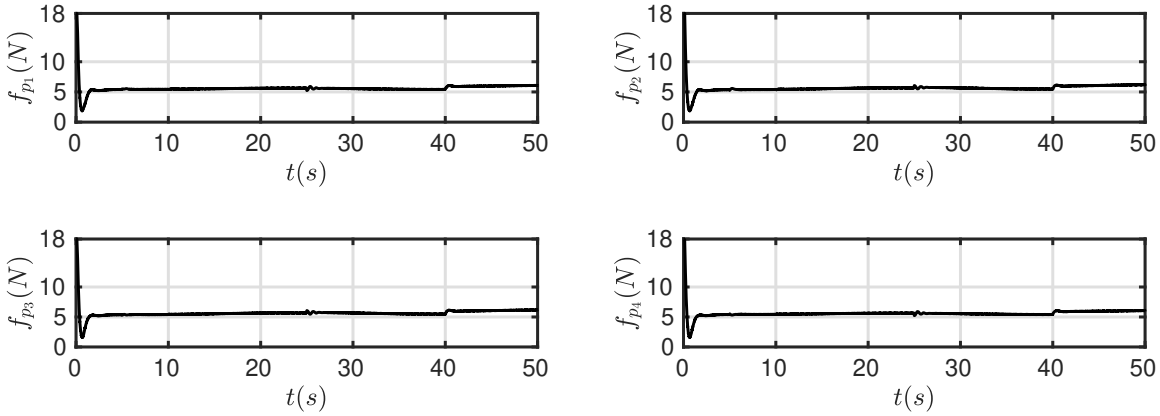

(a) Propellers forces.

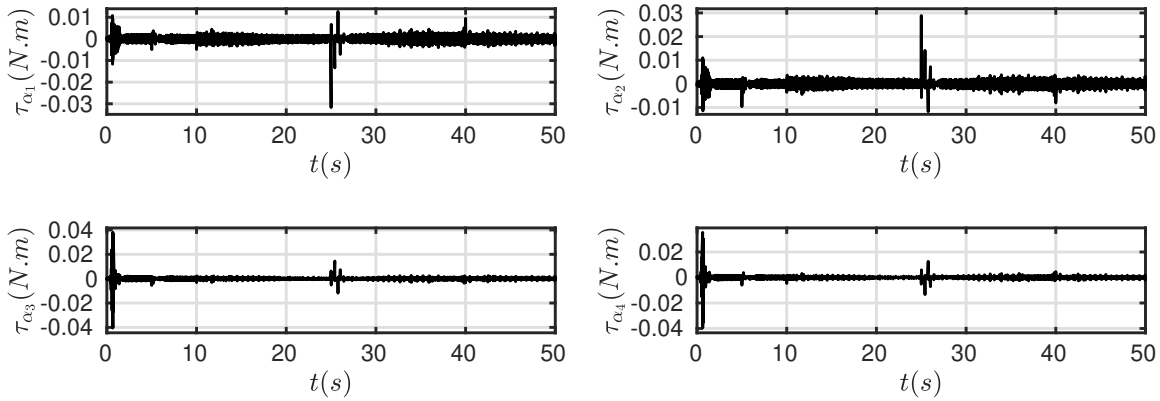

(b) Rotors' torque.

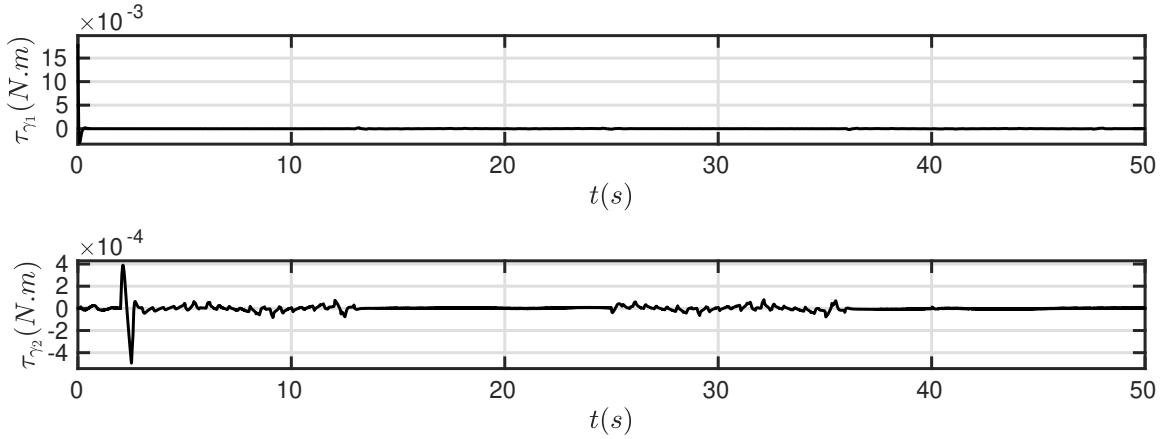

(c) Gimbal torque.

Figure 6 – Control Signals.

References

[1] A. Alkamachi and E. Ercelebi, "Modelling and control of h-shaped racing quadcopter with tilting propellers," *Facta Universitatis, Series: Mechanical Engineering*, vol. 15, no. 2, pp. 201–215, 2017.

[2] N. S. Özbek, M. Önkol, and M. Ö. Efe, "Feedback control strategies for quadrotor-type aerial robots: a survey," *Transactions of the Institute of Measurement and Control*, vol. 38, no. 5, pp. 529–554, 2016.

[3] H. Shraim, A. Awada, and R. Youness, "A survey on quadrotors: Configurations, modeling and identification, control, collision avoidance, fault diagnosis and tolerant control," *IEEE Aerospace and Electronic Systems Magazine*, vol. 33, no. 7, pp. 14–33, 2018.

[4] H. Mo and G. Farid, "Nonlinear and adaptive intelligent control techniques for quadrotor uav–a survey," *Asian Journal of Control*, 2019.

[5] M. Bhargavapuri, J. Patrikar, S. R. Sahoo, and M. Kothari, "A low-cost tilt-augmented quadrotor helicopter: Modeling and control," in *2018 International Conference on Unmanned Aircraft Systems (ICUAS)*. IEEE: IEEE, 2018, pp. 186–194.

[6] S. Bouabdallah and R. Siegwart, "Full control of a quadrotor," in *2007 IEEE/RSJ International Conference on Intelligent Robots and Systems*. IEEE, 2007, pp. 153–158.

[7] G. V. Raffo, "Robust control strategies for a quadrotor helicopter: An underactuated mechanical system," Ph.D. dissertation, Universidad de Sevilla, 2011.

[8] O. Fritsch, P. De Monte, M. Buhl, and B. Lohmann, "Quasi-static feedback linearization for the translational dynamics of a quadrotor helicopter," in *American Control Conference (ACC), 2012*. Montreal: IEEE, 2012, pp. 125–130.

[9] J. Ghandour, S. Aberkane, and J.-C. Ponsart, "Feedback linearization approach for standard and fault tolerant control: Application to a quadrotor uav testbed," in *Journal of Physics: Conference Series*, vol. 570, no. 8. IOP Publishing, 2014, p. 082003.

[10] M. Ryll, H. H. Bülthoff, and P. R. Giordano, "A novel overactuated quadrotor unmanned aerial vehicle: Modeling, control, and experimental validation," *IEEE Transactions on Control Systems Technology*, vol. 23, no. 2, pp. 540–556, 2015.

[11] L. Derafa, A. Benallegue, and L. Fridman, "Super twisting control algorithm for the attitude tracking of a four rotors uav," *Journal of the Franklin Institute*, vol. 349, no. 2, pp. 685–699, 2012.

[12] N. J. S. Amlashi, M. Rezaei, H. Bolandi, and A. K. Sedigh, "Robust second order sliding mode control for a quadrotor considering motor dynamics," *International Journal of Control Theory and Computer Modeling*, vol. 4, no. 1/2, 2014.

[13] B. Barikbin and A. Fakharian, "Trajectory tracking for quadrotor uav transporting cable-suspended payload in wind presence," *Transactions of the Institute of Measurement and Control*, vol. 41, no. 5, pp. 1243–1255, 2019.

[14] H. Castañeda and J. Gordillo, "Spatial modeling, identification and adaptive second order sliding mode control of a micro air vehicle," in *Unmanned Aircraft Systems (ICUAS), 2017 International Conference on*. IEEE: IEEE, 2017, pp. 1083–1091.

[15] F. Muñoz, I. González-Hernández, S. Salazar, E. S. Espinoza, and R. Lozano, "Second order sliding mode controllers for altitude control of a quadrotor uas: Real-time implementation in outdoor environments," *Neurocomputing*, vol. 233, pp. 61–71, 2017.

[16] V. Utkin, J. Guldner, and J. Shi, *Sliding mode control in electro-mechanical systems*. CRC press, 2009.

[17] J. A. Moreno, "Lyapunov approach for analysis and design of second order sliding mode algorithms," in *Sliding Modes after the first decade of the 21st Century*. Springer, 2011, pp. 113–149.

[18] J. A. Moreno and M. Osorio, "A lyapunov approach to second-order sliding mode controllers and observers," in *Decision and Control, 2008. CDC 2008. 47th IEEE Conference on*. IEEE, 2008, pp. 2856–2861.

[19] J. A. Moreno, "A linear framework for the robust stability analysis of a generalized super-twisting algorithm," in *Electrical Engineering, Computing Science and Automatic Control, CCE, 2009 6th International Conference on*. IEEE, 2009, pp. 1–6.

[20] J. C. Vendrichoski, T. L. Costa, E. S. El'Youssef, and E. R. de Pieri, "Mathematical modeling and control of a quadrotor aerial vehicle with tiltrotors aimed for interaction tasks," in *2019 19th International Conference on Advanced Robotics (ICAR)*. IEEE, 2019, pp. 161–166.

[21] T. L. Costa, J. C. Vendrichoski, E. S. El'Youssef, and E. R. De Pieri, "Modeling and control of an unmanned aerial vehicle with tilt rotors equipped with a camera," in *2019 19th International Conference on Advanced Robotics (ICAR)*. IEEE, 2019, pp. 1–6.

[22] R. N. Jazar, *Advanced Dynamics: Rigid body, Multibody, and Aerospace Applications*. Nova Jersey:

John Wiley & Sons, INC, 2011.

[23] S. Boyd, L. El Ghaoui, E. Feron, and V. Balakrishnan, *Linear matrix inequalities in system and control theory*. Siam, 1994, vol. 15.

[24] K. Ogata and Y. Yang, *Modern control engineering*. Prentice hall Upper Saddle River, NJ, 2010, vol. 5.

[25] F. Munoz, M. Bonilla, I. Gonzalez-Hernandez, S. Salazar, and R. Lozano, "Super twisting vs modified super twisting algorithm for altitude control of an unmanned aircraft system," in *Electrical Engineering, Computing Science and Automatic Control (CCE), 2015 12th International Conference on*. IEEE, 2015, pp. 1–6.

Copyright Statement